Tunable Optical Microsystems featuring Vertical Electrostatic Comb Drives

Dissertation submitted to the faculty of Sciences of the University of Neuchâtel, in fulfilment of the requirements for the degree of *"Docteur ès Sciences"*

by

Thomas Overstolz

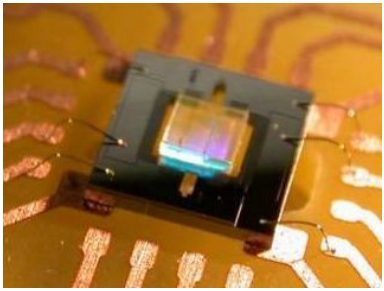

Institute of Microtechnology
University of Neuchâtel
Rue Jaquet-Droz 1
CH-2002 Neuchâtel
Switzerland

2007

Université de Neuchâtel

FACULTE DES SCIENCES
Secrétariat-Décanat de la faculté
Rue Emile-Argand 11
CP 158
CH-2009 Neuchâtel

IMPRIMATUR POUR LA THESE

Tunable Optical Microsystems featuring Vertical Electrostatic Comb Drives

Thomas OVERSTOLZ

UNIVERSITE DE NEUCHATEL

FACULTE DES SCIENCES

La Faculté des sciences de l'Université de Neuchâtel,
sur le rapport des membres du jury

MM. N. de Rooij (directeur de thèse),
H.P. Herzig, W. Noell,
R. Stanley (CSEM, Neuchâtel)
et H. Shea (EPF Lausanne)

autorise l'impression de la présente thèse.

Neuchâtel, le 27 mars 2007

Le doyen :
T. Ward

UNIVERSITE DE NEUCHATEL
FACULTE DES SCIENCES
Secrétariat-décanat de la faculté
Rue Emile-Argand 11 - CP 158
CH-2009 Neuchâtel

Téléphone : +41 32 718 21 00 Fax : +41 32 718 21 03 E-mail : secretariat.sciences@unine.ch www.unine.ch/sciences

Dédié à Stéphanie. Merci pour ton soutien et ta patience.

Meinen Eltern in Dankbarkeit gewidmet.

Keywords

Tunable optical microsystems, SOI, DRIE, HF vapor etching, dicing free chip release, vertical electrostatic comb actuator, tilting platform, torsion beam, resonant grating filter, C-band, piston tip-tilt, tunable cavity, stress compensation, flat mirror

Mots clés

Microsystèmes optiques réglables, SOI, gravure ionique réactive profonde, gravure à vapeur HF, séparation des puces sans sciage, actionneur électrostatique vertical à peigne interdigité, platform pivotable, poudre de torsion, filtre à réseau résonnant, C-band, piston tip-tilt, cavité accordable, compensation de tension, miroir plat

Abstract

This PhD thesis presents the realization of micro electro-mechanical systems for optical applications requiring very precise actuation. One of the requirements was the implementation of a vertical actuation mechanism based on comb actuators that allow accurate static displacements. Two devices have been realized following two different concepts for vertical comb drive actuators.

One device provides a tilting platform of $2\times2\,\mathrm{mm}^2$ which can be used to tune an optical element assembled on top of the platform. Two sets of vertically staggered comb actuators are used to create a vertical force which pulls down the platform to one or to the other side. We achieved a tilt angle of $\pm3.5\,^\circ$ at 80 V in static operation. For demonstration purpose, we assembled a telecom resonant grating filter (RGF) onto the platform. We successfully scanned the entire telecom C-band (1530-1570 nm) by tilting the platform from -3.5 ° to $+3.5\,^\circ$.

The other device provides a triangular mirror of 1.7 mm edge length which is suspended by three C-shaped beams. Three sets of asymmetric vertical comb actuators are used for actuation. The mirror can perform either a pure vertical (piston) displacement of up to 18 µm at 80 V, or a tip-tilt of up to 2.2 mrad at 50 V. The tip-tilt feature allows to correct a small wedge error with an optical component assembled on top of the device. Typical applications of such a device are tunable cavity systems where the required flatness of the mirror is of particular importance.

Contents

Chapter 1

Introduction

This chapter gives an introduction to micro-electro-mechanical systems and microfabrication techniques. Then the topic of this thesis is presented and some state-of-the-art examples are discussed.

1.1 Micro-Electro-Mechanical Systems

The tremendous progress in microelectronics during the last three decades has significantly affected the lifestyle of our generation. The steadily increasing processing power also created a gradually increasing need for sensing real world information including temperature, pressure, acceleration, and force. Solid-state sensor technology with feature sizes in the micrometer range was found to be capable of providing the technical solutions. The downscaling from macroscopic to microscopic dimensions goes ahead with a growing importance of a couple of physical effects that play a minor role in the macroworld. For example, microscopic structures are characterized by a large surface area to volume ratio, and hence surface effects such as electrostatics and wetting dominate volume effects such as inertia or thermal mass.

As the evolution of basic sensor technology continued, more and more complex devices were built containing suspended parts, actuators, and sensing units on the same die. Such complex devices are commonly referred to as micro-electro-mechanical system, or simply MEMS. One example of a typical MEMS mass product can be found in inkjet printers in the print cartridge. The print cartridge contains a series of tiny nozzles each equipped with an electrically heated or piezo actuated membrane that deforms the volume of a small chamber filled with ink, resulting in a small ink bubble being ejected.

MEMS devices have the potential to replace macroscopic systems containing a lot of discrete components, by offering at the same time new functionalities. An example that demonstrates this very nicely is related to accelerometers for airbag activation in cars. Early airbag systems employed at least two electromechanical sensors mounted in the crush zone behind the front bumpers, and one 'safing' sensor located outside the crush zone near the passenger compartment. The sensors employed a proof mass which was pulled out of its mounting in the case of sudden deceleration, closing thus the sensor contact. Today, single point sensing micromachined accelerometers have completely replaced the electromechanical devices. They are directly integrated in the airbag module, reducing thus the number of sensors and associated wiring needed in the system [1]. In contrast to early airbag systems that were activated upon exceeding a trigger value, modern MEMS based accelerometers offer real-time acceleration monitoring and data analysis to determine if and with what level of power the airbag will inflate. A typical accelerometer like the ADXL250 from Analog Device has a full-scale measurement range of $\pm 50\,\mathrm{g}$ ($1\,\mathrm{g} = 9.81\,\mathrm{m/s^2}$) with a resolution of 10 mg, but it can withstand accelerations as high as 2000 g without taking damage [2].

Other even more sophisticated MEMS examples are Lucent's LambdaRouter™ large optical cross-connects, or Texas Instruments Digital Micromirror Device (DMD) which is used in video projectors based on the Digital Light Processor (DLP™) technology [3]. The

DMD device is built up by several layers of structured aluminum and provides a matrix of up to 1 million micromirrors that can individually be actuated. The micromirrors have a size of about 20 µm in square, and the suspension is accomplished with a spring structure that allows deflection of $\pm 10°$. Depending on the actuation state of the individual mirrors, a b/w image is created on the projection screen. Colors are created by placing a color wheel between the projection lamp and the mirror matrix. The color wheel contains three sectors for the primary colors (red, green, blue). The DMD chip is synchronized with the rotating motion of the color wheel such that a sequence of a red, green, and a blue image is created. At a sufficiently high repetition rate, the eye interprets this sequence as the full color image.

1.2 Microfabrication

The term microfabrication designates a fabrication process based on surface or bulk micromachining of a substrate according to patterns that are defined by photolithographic replication from a photomask. For this purpose a spin coated layer of photoresist on top of a substrate is exposed through a mask with UV light. The mask consists typically of a (transparent) quartz or sodalime plate with chromium structures (opaque). In the case positive photoresist, the UV exposed portions become soluble to the developer while the unexposed portions remain insoluble. For negative photoresist, the mechanism is inverted. The patterns thus created in the photoresist are transferred into the substrate by etching the uncovered substrate, while the remaining photoresist structures act as an etch protection.

The fabrication of MEMS devices is based on either surface micromachining or bulk micromachining, or a combination of the two. In surface micromachining, thin polysilicon or metal layers are consecutively deposited and structured. Complex structures, such as movable parts, are built using a sacrificial layer, which is selectively removed once the structural layer on top of the sacrificial layer is

patterned. Typically, surface micromachined devices combine thin structures with small feature sizes, and hence they are characterized by quite high resonance frequencies. An important benefit of surface micromachining is its compatibility with CMOS processing, i.e. mechanical and electronical building blocks can simultaneously be fabricated next to each other on the same substrate. On the other side, surface micromachined devices suffer from poor rigidity, which can be problematic especially for optical applications like scanners, because the deformation under acceleration of optical relevant components is not acceptable. A typical device based on surface micromachining is the Texas Instruments DMD used in video projectors [3].

Unlike surface micromachining, which uses a succession of thin film deposition and selective etching, bulk micromachining defines structures by selectively etching inside a substrate. Bulk micromachining is based on wet or dry etching of single-crystal silicon substrates with thicknesses of up to several hundreds of micrometers. Wet chemical etching based on acidic solvents can be used for isotropic etching, whereas the use of alkaline solvents such as potassium hydroxide (KOH) or TMAH results in anisotropic etching. Alkaline solvents dissolve the silicon in a highly anisotropic way, with some crystallographic orientations dissolving up to 1000 times faster than others [4]. Dry etching of single-crystal silicon, the so-called deep reactive ion etching (DRIE), is performed in a reaction chamber using plasma of a reactive gas. In contrast to anisotropic wet chemical etching, the anisotropy in DRIE is independent of the crystallographic orientations of the lattice, a fact that is crucial for anisotropically etching arbitrary shaped structures. On the other hand, wet chemical etching is a batch process which makes it interesting for mass production.

Microfabrication is characterized by massive parallel processing where several hundred up to several thousand devices on one wafer are fabricated at once. All devices on the wafer undergo the exact same fabrication steps with the same parameters, although many processes do not produce fully uniform results across the wafer. Nev-

ertheless, the repeatability of the device characteristics is in general excellent and tolerances can be maintained small.

1.3 Mechanical Properties of Silicon

Besides the well-established semiconducting characteristics, silicon has excellent mechanical properties that make it suitable as a building material for miniaturized mechanical systems [5]. Compared to steel, single-crystal silicon has similar elasticity, but its yield strength is higher and its specific weight is lower than that of steel. As a result, the moment of inertia is reduced, a fact that is particularly interesting for mechanical systems subject to acceleration. For example, Perret *et al.* reported on an innovative escape mechanism fabricated in single-crystal silicon and used in the Ulysse Nardin "Freak" wristwatch [6]. In this application, the reduced moment of inertia yields in a highly shock insensitive component which easily withstands several thousands of g, and the low inertia also reduces the energy consumption considerably. Micromachined parts in single-crystal silicon have very smooth surfaces resulting in a very low friction coefficient which reduces mechanical losses. MEMS devices produced in crystalline silicon are very robust and durable and material fatigue does not occur due to the single crystalline structure of silicon.

1.4 Objectives

Many applications in optics require small and accurate tunable components. These components could potentially be used for optical switching, beam steering, or cavity tuning, but also for angular, lateral, or vertical positioning of optical elements such as filters or lenses. MEMS devices providing optical functionalities, so-called optical MEMS, are widely considered to feature the desired requirements in terms of size, speed, planarity, surface smoothness, relia-

bility, and tunability.

The topic of this PhD thesis is the development and realization of MEMS devices providing a vertical actuation mechanism for tuning purpose of optical elements. The vertical actuation mechanism will complement the electrostatic comb actuators providing lateral actuation that have been developed earlier [7] at the Institute of Microtechnology of the University of Neuchâtel.

Based on the vertical actuation mechanism, two different devices will be realized in the context of this work. One device will provide a single-axis tilting platform that can be assembled with an optical element which is characterized by an angular functionality. By slowly tilting the platform, the optical element can be tuned. Alternatively, a mirror can be implemented instead of the platform. The tilting platform is specified to measure $2\times2\,\mathrm{mm}^2$, with a target mechanical tilt angle of $\pm4^\circ$. The platform has to be equipped with a large through hole for optical transmission. A demonstrator will be set up to show the angle tunability of the platform. For this purpose, a telecom resonant grating filter (RGF) will be assembled onto the platform. The wavelength of the RGF's reflection peak can be shifted by changing the angle of incidence, i.e. by tilting the platform.

The second device will provide a piston tip-tilt mirror. Typical applications of such a device are tunable cavity systems such as interferometers, tunable lasers, and filters. Common to all these applications is the required flatness of the mirror. The target piston displacement is in the order of $10\,\mu\mathrm{m}$, while the tip-tilt can be very small.

1.5 State of the Art

In this section some devices known as scanning micromirrors are discussed. Scanning micromirrors are typically operated dynamically in resonance rather than statically and achieve thus higher amplitudes with less excitation energy. Despite the target of this work that

aims to develop devices featuring tunability and thus small static motions, the comparison with scanning micromirrors is interesting because they also require a vertical actuation mechanism. Several research groups have successfully demonstrated scanning micromirrors using various actuation mechanisms, including thermomechanical, piezoelectric [8], electromagnetic [9–11], and electrostatic actuation [12–17].

Thermomechanical actuators, however, are less suited for optical applications since the heat generation leads to unwanted curvature of the reflective surface and affects strongly the refractive index of optical components.

Piezoelectric actuators offer a large force density at low actuation voltage, but the fabrication process is relatively complex. Piezoelectric actuators based on lead zirconate titanate (PZT) thin films require structural deformation during actuation, which makes them the ideal candidate for cantilever actuation [18]. An interesting approach for creating rotational motion is presented by Tani *et al.* who use two piezoelectric bimorph actuators located to the right and the left side of a beam and operated such that half of the beam bends upward and half of the beam bends downwards. The coupled bending motions result in a pure torque in the middle of the beam [8].

Electromagnetic actuators provide relatively large torque at small voltage. The need for permanent magnets makes this type of actuator quite bulky, and the integration of a coil is space consuming and complicates the fabrication process. Despite this inconveniences, electromagnetic actuators are used mainly in optical scanners, where the need of large surface for the coil can be combined with the large scanning mirror surface required to minimize diffraction. Examples of commercially available optical scanners with electromagnetic actuators can be found in Olympus' OLS1200 confocal laser scanning microscope [10], or in Microvision's Nomad biaxial retinal scanner display [11].

Electrostatic actuators have become a key component in the domain of MEMS. This type of actuator is characterized by an extremely low power consumption compared to other type of actua-

tors, and its implementation is simple. The generated electrostatic forces are, though small, highly sufficient to move small and lightweight parts on a MEMS device. In contrast to the well known comb drive actuators that are used for lateral actuation in the xy-plane, vertical comb drive actuators allow vertical or out of plane motion. Early vertical comb-drive actuators reported by Yeh *et al.* are based on the combination of silicon bulk micromachining and polysilicon surface micromachining. Compared to parallel-plate actuators, the achieved total vertical displacement is higher while the required operating voltage for an identical displacement is lower. However, the vertical displacement is limited by the thickness of the polysilicon layer and reaches no more than a few micrometers [17]. Silicon-on-insulator (SOI) wafers with a significantly thicker device layer have become the preferred choice for attaining large vertical displacements. For example, Tsuboi *et al.* realized a scanning mirror device based on vertically staggered comb electrodes that are located in the device and the handle layer of a SOI substrate [13, 19]. The mirror is supported using two torsion bars at either side of the mirror that are arranged such that they form the shape of a V (top-view), with the associated end being connected to the anchor. The use of such V-shaped torsion bars instead of simple straight torsion bars increases drastically the lateral stability of the mirror at high actuation voltages. As a result, a misalignment of up to 2 µm between the comb actuators in the device and in the handle layer can be accepted without running the risk of stiction due to the occurrence of parasitic lateral forces.

Other research scientists tend to solve the problem of misalignment rather than trying to reinforce the lateral stability of torsion bars. Krishnamoorthy *et al.* described a self-alignment fabrication process that minimizes misalignment of vertically staggered electrostatic combdrives created in the device and the handle layer of an SOI wafer [14]. The process consists in using an additional set of static combs in the device layer as a mask to structure the subjacent handle layer. Kwon *et al.* reported on a method that features the fabrication of self-aligned and pre-engaged vertical comb actuators

in only the device layer of a SOI wafer [15]. The process employs a stack of two oxide masks on top of each other and allows basically to reduce selectively the height of one comb of the comb pair, while maintaining the original height of the other comb. By providing two comb pairs with alternating height levels of the mobile and the static comb, respectively, bidirectional upward and downward piston motion is possible.

A completely different approach for the realization of vertical comb actuators consists in fabricating the comb pair initially on the same level, but vertically relocate one of the combs afterwards. For example, Fujino *et al.* reported on a method where the mobile comb of a comb pair is lifted up on one side by 6-8° using a thermal reflow and shrinking process of photodefinable benzocyclobutene which is applied after DRIE but prior to etching the buried oxide [12]. A similar method proposed by Sasaki *et al.* uses stress induced composite bridges to lift up a suspended mobile structure through a buckling effect [16].

1.6 Choice of Technology

The devices realized in the context of this work are based on DRIE processing of SOI substrates, and the actuation mechanism is accomplished using vertical electrostatic comb drives. The choice for SOI technology was motivated by the relative simple fabrication technique involving only few process steps, but also by the excellent mechanical and optical properties of single-crystal silicon. There is also an observable trend in the international scientific community towards this technique, especially for optical applications [20].

The concept of vertically staggered electrostatic comb drives based on SOI technology featuring potentially large vertical displacements was new in spring 2001, when this work started, and to the knowledge of the author no work on this topic was published before.

1.7 Outline

Chapter 1 gives an introduction to microfabricated miniaturized mechanical systems in single-crystal silicon. The different technologies of state-of-the-art optical MEMS are discussed in order to situate the work and to outline the objectives. Chapter 2 introduces the mechanical and the electrostatic theory. Based on the electrostatic theory an analytically approximated model is developed that allows to calculate the electrostatic force. In Chapter 3 the device concept is presented, and the different device parameters are evaluated. Based on the established model, the characteristics of the device are predicted. Chapter 4 describes the fabrication of the device. Chapter 5 presents the mechanical and optical measurement results and compares them with theory. Finally, the work is concluded.

Bibliography

[1] M. J. Madou, *Fundamentals of Microfabrication*, p. 464. CRC Press, first edition, 1997, ISBN 0-8493-9451-1.

[2] Analog Devices, Inc., Norwood (MA), United States, *ADXL150/ADXL250 Data Sheet*.
URL `http://www.datasheetcatalog.com/datasheets_pdf/A/D/X/L/ADXL250.shtml`

[3] L. J. Hornbeck, "Digital Light Processing™: A New MEMS-Based Display Technology". *Texas Instruments White Paper Library*, 1995.
URL `http://dlp.com/dlp_technology/dlp_technology_white_papers.asp`

[4] H. Seidel, L. Csepregi, A. Heuberger, and H. Baumgärtel, "Anisotropic etching of crystalline silicon in alkaline solutions". *J. Electrochem. Soc.*, **137**(11):3612–3626, 1990.

[5] K. E. Petersen, "Silicon as a mechanical material". *Proceedings of the IEEE*, **70**:420–457, May 1982.

[6] A. Perret, A. Hoogerwerf, P. Niedermann, X.-M. Tang, S. Jeanneret, P.-A. Clerc, N. F. de Rooij, and P. Gygax, "Silicon as material for mechanical wristwatches". In "Design, Test, Integration, and Packaging of MEMS/MOEMS", volume 4755, pp. 645–647, SPIE, 2002.
URL `http://link.aip.org/link/?PSI/4755/645/1`

[7] V. P. Jaecklin, C. Linder, N. F. de Rooij, and J.-M. Moret, "Micromechanical comb actuators with low driving voltage". *J. Micromech. Microeng.*, **2**(4):250–255, 1992.

[8] M. Tani, M. Akamatsu, Y. Yasuda, H. Fujita, and H. Toshiyoshi, "A 2D-Optical Scanner Actuated by PZT Film Deposited by Arc Discharged Reactive Ion-Plating (ADRIP) Method". In "Proc. IEEE/LEOS Int. Conf. on Optical MEMS", pp. 188–189, Aug. 22-26 2004.

[9] C.-H. Ji, S.-H. Ahn, K.-C. Song, H.-K. Yoon, M. Choi, S.-C. Kim, and J.-U. Bu, "Dual-Axis Electromagnetic Scanning Micromirror using Radial Magnetic Field". In "Digest 19th IEEE Int. Conf. on Micro Electro Mechanical Systems", pp. 32–35, 2005.

[10] H. Miyajima, N. Asaoka, T. Isokawa, M. Ogata, Y. Aoki, M. Imai, O. Fujimori, M. Katashiro, and K. Matsumoto, "MEMS Electromagnetic Optical Scanner for a Commercial Confocal Laser Scanning Microscope". *IEEE J. Microelectromechanical Systems*, **12**(3):243–251, June 2003.

[11] H. Urey, F. A. DeWitt, P. A. Lopez, and J. Tauscher, "MEMS raster correction scanner for SXGA resolution retinal scanning display". In "MOEMS Display and Imaging Systems", volume 4985, pp. 106–114, SPIE, 2003.
URL `http://link.aip.org/link/?PSI/4985/106/1`

[12] M. Fujino, P. R. Patterson, H. Nguyen, W. Piyawattanametha, and M. C. Wu, "Monolithically Cascaded Micromirror Pair Driven by Angular Vertical Combs for Two-Axis Scanning". *IEEE J. Select. Topics Quantum Electron.*, **10**(3):492–497, May/June 2004.

[13] O. Tsuboi, Y. Mizuno, N. Koma, H. Soneda, H. Okuda, S. Ueda, I. Sawaki, and F. Yamagishi, "A Rotational Combdriven Micromirror with a Large Deflection Angle and Low Drive Voltage". In "Digest 15th IEEE Int. Conf. on Micro Electro Mechanical Systems", pp. 532–535, 2002.

[14] U. Krishnamoorthy, L. Daesung, and O. Solgaard, "Self-aligned vertical electrostatic combdrives for micromirror actuation". *IEEE J. Microelectromechanical Systems*, **12**(4):458– 464, August 2003.

[15] S. Kwon, V. Milanovic, and L. P. Lee, "Large-Displacement Vertical Microlens Scanner with Low Driving Voltage". *IEEE Photonics Technology Letters*, **14**(11):1572–1574, November 2002.

[16] M. Sasaki, D. Briand, W. Noell, N. F. de Rooij, and K. Hane, "Three-Dimensional SOI-MEMS Constructed by Buckled Bridges and Vertical Comb Drive Actuators". *IEEE J. Select. Topics Quantum Electron.*, **10**(3):455–461, May/June 2004.

[17] J.-L. A. Yeh, H. Jiang, and N. C. Tien, "Integrated Polysilicon and DRIE Bulk Silicon Micromachining for an Electrostatic Torsional Actuator". *IEEE J. Microelectromechanical Systems*, **8**(4):456–465, December 1999.

[18] P. Luginbuhl, G.-A. Racine, P. Lerch, B. Romanowicz, K. Brooks, N. de Rooij, P. Renaud, and N. Setter, "Piezoelectric Cantilever Beams Actuated by PZT Sol-Gel Thin Film". *Sensors and Actuators*, **A54**(1-3):530–535, June 1996.

[19] O. Tsuboi, S. Ueda, Y. Mizuno, I. Sawaki, and H. Okuda, "Micromirror unit with torsion connector having nonconstant width". US Patent 6,795,225, September 2004.

[20] V. A. Aksyuk, F. Pardo, D. Carr, D. Greywall, H. B. Chan, M. E. Simon, A. Gasparyan, H. Shea, V. Lifton, C. Bolle, S. Arney, R. Frahm, M. Paczkowski, M. Haueis, R. Ryf, D. T. Neilson, J. Kim, C. R. Giles, and D. Bishop, "Beam-Steering Micromirrors for Large Optical Cross-Connects". *Journal of Lightwave Technology*, **21**(3):634–642, March 2003.

Chapter 2

Theory

In this chapter the electrostatic theory and the beam theory are introduced. Based on the electrostatic theory the force achieved with vertical electrostatic comb actuators is calculated. The beam theory provides a method to calculate the restoring force of a deformed spring. Combining both theories allows us to establish the relation between displacement and actuation voltage.

2.1 Electrostatic Actuation

2.1.1 Charge and Electric Field

Gauss' law describes the relation between the electric flux flowing out a closed surface and the electric charge enclosed in the surface. In its integral form, Gauss's law writes

$$\oint_S \boldsymbol{D} \cdot d\boldsymbol{A} = \int_V \rho \cdot dV \tag{2.1}$$

where ρ is the free electric charge density, and $\boldsymbol{D}$ is the electric displacement field. The electric displacement field $\boldsymbol{D}$ is related to

the electric field by $\boldsymbol{D} = \epsilon_0 \epsilon_r \boldsymbol{E}$ with ϵ_0 being the permittivity of free space, and ϵ_r being the dielectric constant. Hence, the electric field $\boldsymbol{E}$ can be expressed as

$$\boldsymbol{E} = \frac{Q}{\epsilon_0 \epsilon_r A \hat{\boldsymbol{n}}}, \tag{2.2}$$

where the direction of $\boldsymbol{E}$ is parallel to the normal unit vector $\hat{\boldsymbol{n}}$ of the surface A. It becomes obvious that the appearance of charge is always accompanied by an electric field. On the other hand, the electric field can always be expressed as the gradient of a potential V:

$$\boldsymbol{E} = -\vec{\text{grad}}\, V \tag{2.3}$$

Lets consider the electric field between two conducting parallel plates with surface A that are separated by a distance d. In this particular configuration the electric field becomes homogeneous, and Eq. 2.3 writes

$$E_x = -\frac{dV}{dx} = \frac{V}{d}. \tag{2.4}$$

If the surface A of the two parallel plates in Fig. 2.1 is large compared to the separation gap d, the inhomogeneous electric field created at

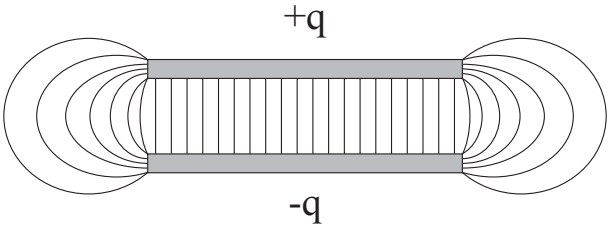

Figure 2.1: *Two charged parallel conductors and the corresponding electric field. The electric field inside the two parallel plates is homogeneous, whereas it is inhomogeneous outside.*

the edges of the plates can be neglected. Combining Eq. 2.4 and Eq. 2.2 and solving for the charge Q yields

$$Q = \frac{\epsilon_0 \epsilon_r A}{d} \cdot V \tag{2.5}$$

The fraction to the right hand side of Eq. 2.5 is defined as the capacity C:

$$C = \epsilon_0 \epsilon_r \frac{A}{d} \tag{2.6}$$

It indicates how many charges can be accumulated and depends only on the geometry of the plates. An element with the ability to store charges is called a capacitor.

2.1.2 Energy and Force of a Capacitor

A capacitor stores energy in the electric field between its two charged terminals. In order to transfer an infinitesimal amount of charge dq against the potential V from one terminal to the other, the required energy dU is expressed by

$$dU = dq \cdot V. \tag{2.7}$$

Using Eq. 2.5 with 2.6, the total energy calculates

$$U = \frac{1}{C} \int Q dQ = \frac{1}{2C} Q^2 = \frac{1}{2} C V^2. \tag{2.8}$$

The electrostatic force $\boldsymbol{F_E}$ between the two electrodes of a charged capacitor is given by the gradient of the energy:

$$\boldsymbol{F_E} = - \vec{grad}\, U \tag{2.9}$$

2.1.3 Parallel Plate Actuator

In the case of the capacitor in Fig. 2.2 representing a parallel plate actuator, we assume that the mobile plate suspended by the spring only moves in z-direction under the influence of a force created by the applied potential. In this case, the gradient of the energy becomes one-dimensional:

$$F_E = -\frac{1}{2}\frac{\partial C}{\partial z}V^2 \tag{2.10}$$

For a parallel plate actuator with an edge length of 1000 µm, an electrode spacing of 10 µm, and an applied potential of 100 V, the force produced between the two electrodes has a value of 442.5 µN. In practice, parallel plate actuators like the one depicted in Fig. 2.2

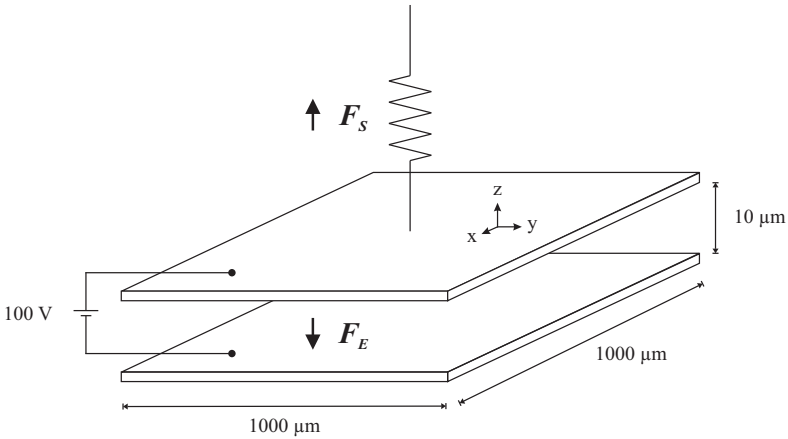

Figure 2.2: *A potential difference applied to two conductive plates creates an attractive force between them. In a set-up where one of the two plates is fixed and the other plate is suspended by a spring, the attractive force results in a displacement of the suspended plate towards the fixed plate.*

have a limited range of operation due to the pull-in phenomenon [1]. The problem also occurs from Eq. 2.10. For decreasing distance z between the two electrode plates, the force increases with the power of two. This suggests that for a given distance z, the electrostatic force between the two electrode plates becomes dominant over the spring force and the two electrode plates get in uncontrolled close contact. The pull-in phenomenon can be avoided if the actuator is only operated in 1/3 of the full range distance. In the example depicted in Fig. 2.2, the parallel plate actuator could be actuated from the initial 10 µm gap distance to a gap distance of 6.5 µm without running the risk of pull-in.

2.1.4 Comb Actuators for In-Plane Motion

An improvement over electrostatic parallel plate actuators are the so-called electrostatic comb drive actuators. They consist of a set of static combs and a set of mobile combs, which are interdigitated. Electrostatic comb drive actuators result typically in an in-plane motion [2, 3], where the mobile comb is attracted by the static comb. The arrangement is depicted in Fig. 2.3. In order to calculate the force according to Eq. 2.9, the formula for the capacity in function

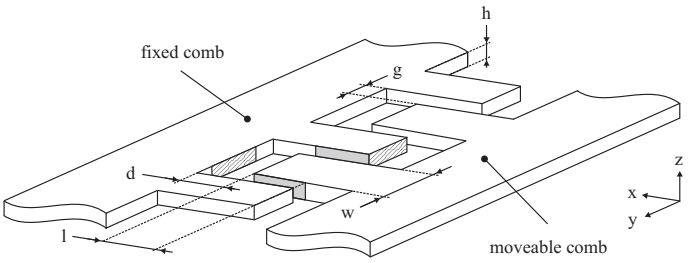

Figure 2.3: *Typical comb actuator containing a fixed comb and a mobile comb. The suspension of the mobile comb has to ensure that only displacements in x-direction are possible.*

of the displacement has to be established. From Fig. 2.3 one can see that the comb structure is periodical. One period is composed of two times two types of surfaces, the hatched surface and the grey surface. While the hatched surface does not change in function of the x-displacement of the mobile comb, the grey surface does. Accordingly, the capacity of one period can be written as

$$C = 2\,\epsilon_0\epsilon_r \left(\frac{h \cdot (l+x)}{g} + \frac{w \cdot h}{d-x} \right) \tag{2.11}$$

In practice, the width w of the combs is much smaller than the length l, and the gap g between the combs is much smaller than the gap d at the end of the combs. Therefore, the second term in the parenthesis of Eq. 2.11 can be neglected. Hence, the achieved electrostatic force is expressed by

$$F_E = -\frac{1}{2}\frac{\partial C}{\partial x} N V^2 = -\epsilon_0\epsilon_r \frac{h}{g} N V^2 \tag{2.12}$$

where N is the number of mobile combs. The fact that the force created at the hatched end surface of the combs is negligible explains why the pull-in phenomenon does not occur in this type of actuators, as long as $d >> g$. Therefore, comb drive actuators are well suited for actuation ranges of up to several hundreds of micrometers [4].

2.1.5 Comb Actuators for Out-of-Plane Motion

A. Vertically Staggered Comb Drive

The configuration of in-plane comb drive actuators discussed in Sec. 2.1.4 can be modified to realize an out-of-plane comb drive actuator. This is achieved by vertically displacing the static comb such that a stack of two levels is created, with the mobile comb being on one level, and the static comb on the other. In practice it is more convenient to add another static comb underneath the existing static comb, as depicted in Fig. 2.4. Vertical displacement of the mobile comb is achieved by applying a potential between the mobile comb

and the bottom static comb. The energy stored on the variable capacitor formed by the mobile and the static comb is again a function of the overlap surface which changes in function of immersion depth.

Depending on the suspension concept of the mobile part with the mobile combs, vertically staggered comb drive actuators can be used to create either a parallel vertical displacement, or a tilt around an axis. The latter case is depicted in Fig. 2.5. The common area between one static and one mobile comb is given by

$$A = \int_{R}^{y_0} z_1(y)dy + \int_{y_0}^{y_e} z_2(y)dy - (y_e - R) \cdot b \tag{2.13}$$

where

$$\begin{aligned} z_1(y) &= \tan\theta \cdot y + b, \\ z_2(y) &= -\frac{1}{\tan\theta} \cdot y + c \end{aligned} \tag{2.14}$$

The constant b can be retrieved from the initial unactuated state

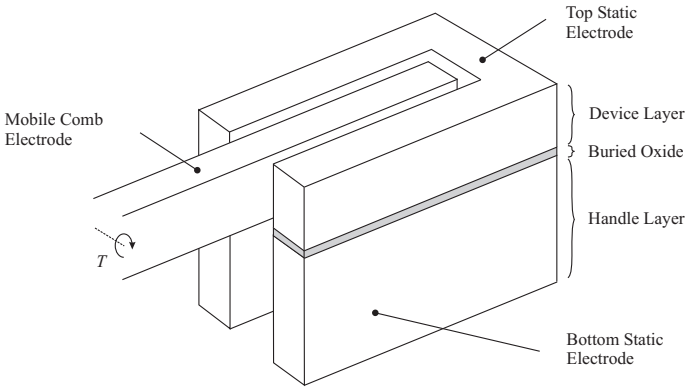

Figure 2.4: *Adding a bottom static comb underneath the top static comb results in an out-of-plane comb drive actuator.*

of the platform where $\theta = 0$. In this case

$$b = \frac{h}{2}, \tag{2.15}$$

since the axis of rotation is located at half the height of the platform. The constant c is obtained by intersecting the two lines z_1 and z_2 at y_0:

$$\begin{aligned} z_1(y_0) &= z_2(y_0) \\ \tan\theta \cdot y_0 + b &= -\frac{1}{\tan\theta} \cdot y_0 + c \end{aligned} \tag{2.16}$$

Solving Eq. 2.16 for c yields

$$c = y_0 \cdot \left(\tan\theta + \frac{1}{\tan\theta} \right) + b \tag{2.17}$$

Let's evaluate the limits of the two integrals in Eq. 2.13. The lower bound limit of the first integral is given by the edge R of the platform. The upper bound limit of the first integral and the lower bound limit of the second integral, y_0, is given by

$$y_0 = (R + r) \cdot \cos\theta - b \cdot \sin\theta \tag{2.18}$$

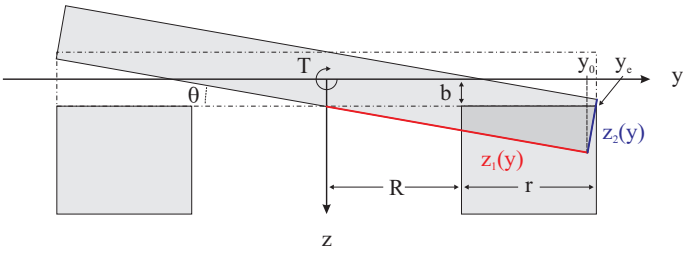

Figure 2.5: *Model to calculate the dark grey surface in function of increasing tilt angle θ. This surface represents the common surface between one static (backside) comb and one mobile comb.*

The upper bound limit of the second integral, y_e, is obtained by intersecting the line $z = b$ with $z_2(y_e)$:

$$\begin{aligned} z_2(y_e) &= b \\ &= -\frac{1}{\tan\theta} \cdot y_e + y_0 \cdot \left(\tan\theta + \frac{1}{\tan\theta}\right) + b = b. \end{aligned} \tag{2.19}$$

Solving Eq. 2.19 for y_e yields

$$y_e = y_0 \cdot (1 + \tan^2\theta) \tag{2.20}$$

Let's evaluate separately the two integrals in Eq. 2.13.

$$\begin{aligned} A_1 &= \int_R^{y_0} z_1(y)dy = \int_R^{y_0} (\tan\theta \cdot y + b)dy \\ &= \frac{1}{2}\tan\theta \cdot {y_0}^2 - \frac{1}{2}\tan\theta \cdot R^2 + b \cdot y_0 - b \cdot R \end{aligned} \tag{2.21}$$

$$\begin{aligned} A_2 &= \int_{y_0}^{y_e} z_2(y)dy = \int_{y_0}^{y_e} \left(-\frac{1}{\tan\theta} \cdot y + c\right)dy \\ &= \frac{1}{2}\frac{1}{\tan\theta} \cdot {y_0}^2 - \frac{1}{2}\frac{1}{\tan\theta} \cdot {y_e}^2 + c \cdot y_e - c \cdot y_0 \end{aligned} \tag{2.22}$$

By replacing c and y_e in Eq. 2.22 with their corresponding expression derived in Eq. 2.17 and Eq. 2.20, respectively, the surface A_2 can be rewritten as

$$A_2 = \frac{1}{2}{y_0}^2 \tan^3\theta + b\, y_0 \tan^2\theta \tag{2.23}$$

Eq. 2.13 can now be rewritten using Eq. 2.21 and Eq. 2.23:

$$\begin{aligned} A &= A_1 + A_2 - (y_e - R) \cdot b \\ &= \frac{1}{2}\tan\theta \cdot {y_0}^2 - \frac{1}{2}\tan\theta \cdot R^2 + \frac{1}{2}{y_0}^2 \tan^3\theta \\ &\quad + b \cdot \underbrace{y_0(1+\tan^2\theta)}_{y_e} - b \cdot R - (y_e - R) \cdot b \\ &= \frac{1}{2}{y_0}^2 \tan\theta(1+\tan^2\theta) - \frac{1}{2}R^2\tan\theta. \end{aligned} \tag{2.24}$$

Replacing y_0 by the expression derived in Eq. 2.18 yields finally the surface A of the overlap area between one mobile and one static comb in function of the tilt angle θ:

$$A = \frac{1}{2}(2Rr + r^2)\tan\theta - \frac{1}{2}(R+r)h\tan^2\theta + \frac{1}{8}h^2\tan^3\theta \tag{2.25}$$

The second and third order terms in Eq. 2.25 can be neglected without much loss of accuracy. Indeed, the second order term is more than a factor 1000 smaller than the first order term. The simplified formula for the surface between one mobile and one static comb in function of the tilt angle θ is then given by

$$A \approx \frac{1}{2}(2Rr + r^2)\tan\theta \tag{2.26}$$

Accordingly, the capacity per unit comb writes

$$C \approx \frac{\epsilon_0\epsilon_r(2Rr + r^2)}{g} \cdot \tan\theta \tag{2.27}$$

where g denotes the gap between a mobile and a static comb. For small angles θ, the simplified capacity per unit comb writes

$$C \approx \frac{\epsilon_0\epsilon_r(2Rr + r^2)}{g} \cdot \theta \tag{2.28}$$

B. Asymmetric Vertical Comb Drive

Another type of comb actuator for out-of-plane motion is based on static and mobile combs of different height that are offset in the initial position, as depicted in Fig. 2.6. In such a configuration the calculus of the force is difficult since the common area between mobile and static combs is always constant and no surface change occurs as a function of vertical displacement. The vertical force has its origin in the asymmetric arrangement of the combs and in the resulting inhomogeneous electric field. Although the inhomogeneous electric field is in general small compared to the homogenous electric field, it can not be neglected in this case since only the inhomogeneous electric field is subject to variations, whereas the homogeneous electric field is always constant. Yeh *et al.* presented an approximated analytical solution to calculate the force in the inhomogeneous electric field by reducing the 3D space of the electric field to a 1D problem [5]. However, the method only considers the electric field between two parallel combs and fails as soon as the electric field is influenced by other geometries like a grounded substrate underneath the combs.

For this reason, we did not try to establish an analytical model but rather evaluated the attainable force in the inhomogeneous elec-

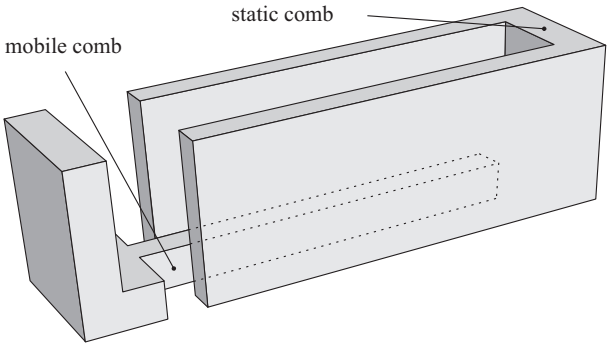

Figure 2.6: *Asymmetric vertical comb actuator.*

tric field using FEM modeling. This part of the work is presented in Sec. 3.2.5.

2.2 Mechanical Suspension

2.2.1 Suspension Concepts

In MEMS devices, mobile parts are suspended by thin and flexible beams to a stable island, the so-called anchor. The beams constitute mechanical springs, and the mechanical restoring force of the beams increases upon mechanical deformation. The arrangement and the shape of the beams has to be chosen such that they are soft in a preferred direction of actuation, but stiff for deformation in other directions. In the following sections, the two basic suspension concepts used for the realized devices are presented.

2.2.2 Bending of a Beam

The bending of a beam under the influence of load goes ahead with a proportional increase of the potential energy. This mechanical

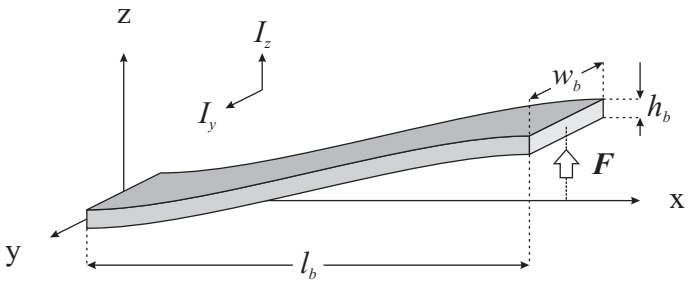

Figure 2.7: *Deflection of a beam under load, with one end fixed and one end guided. The area moment of inertia depends on the direction of deflection.*

energy U_M is given by

$$U_M = \frac{1}{2} k_b \, z^2 \tag{2.29}$$

where k_b designates the spring constant, and z the displacement. The applied load is related to the energy by its derivative:

$$F_M = -\frac{\partial U}{\partial z} = -k_b \, z \tag{2.30}$$

In the case of a leaf spring of length l_b and rectangular cross section of width w_b and height h_b, the spring constant k_b is given by [6]

$$k_b = \frac{12EI}{{l_b}^3} \tag{2.31}$$

where E designates Young's Modulus, and I denotes the area moment of inertia. The area moment of inertia measures the direction dependent resistance of a shape to bending and deflection. In the case where the beam is deflected into z-direction (Fig. 2.7), the corresponding area moment of inertia I_z calculates according to

$$I_z = \int z^2 dA \tag{2.32}$$

For a beam with rectangular cross section of width w_b and height h_b, the area moment of inertia I_z writes

$$I_z = \int_{-w_b/2}^{w_b/2} dy \int_{-h_b/2}^{h_b/2} z^2 dz = \frac{w_b \cdot {h_b}^3}{12} \tag{2.33}$$

2.2.3 Torsion of a Beam

The torsional deformation of a spring under the influence of torque yields in an increase of strain energy. The mechanical energy U_M

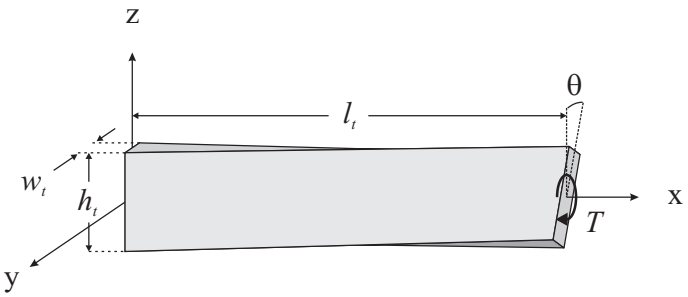

Figure 2.8: *Torsion of a beam as a result of applied torque.*

in the system can be expressed quite similarly to the case of the deflected bending beam, i.e.

$$U_M = \frac{1}{2} k_t \, \theta^2 \tag{2.34}$$

where k_t designates the torsional spring constant, and θ the angle of twist between the two extremities of the spring. The applied torque is quantified by the derivative of the energy:

$$T_M = -\frac{\partial U}{\partial \theta} = -k_t \, \theta \tag{2.35}$$

In the case of a leaf spring of length l_t having a rectangular cross section of width w_t and height h_t, the spring constant k_t is given by [7]

$$k_t = \frac{G \, h_t \, {w_t}^3}{3 \, l_t} \left(1 - \frac{192}{\pi^5} \frac{w_t}{h_t} \right), \; h_t > w_t \tag{2.36}$$

where G denotes the modulus of rigidity.

2.3 Electro-Mechanical Analysis

In the previous two sections we have quantified, respectively, the electrostatic energy U_E of a comb drive actuator, and the potential

energy U_M of a mechanically deformed spring. A simplified analysis of the coupled electro-mechanical system neglecting damping effects can be obtained by equalizing the energies involved:

$$U_M - U_E = 0 \tag{2.37}$$

Alternatively, the derivative of the energy representing the force and the torque, respectively, can be used to calculate the equilibrium state. The electro-mechanical analysis allows us to establish the relation between the mechanical displacement and the actuation voltage.

Bibliography

[1] O. Degani, E. Socher, A. Lipson, T. Leitner, D. J. Setter, S. Kaldor, and Y. Nemirovsky, "Pull-In Study of an Electrostatic Torsion Microactuator". *IEEE J. Microelectromechanical Systems*, **7**(4):373–379, 1998.

[2] O. Manzardo, H. P. Herzig, C. Marxer, and N. F. de Rooij, "Miniaturized time-scanning Fourier transform spectrometer based on silicon technology". *OPTICS LETTERS*, **24**(23):1705–1707, 1999.

[3] C. Marxer and N. F. de Rooij, "Micro-optomechanical 2 x 2 switch for single-mode fibers based on a plasma-etched silicon mirror and electrostatic actuation". *Journal of Lightwave Technology*, **17**(1):2–6, 1999.

[4] O. Manzardo, F. Schädelin, W. Noell, N. F. de Rooij, and H. P. Herzig, "Infrared MEMS-based Lamellar grating spectrometer". In "MEMS, MOEMS, and Micromachining", volume 5455, pp. 1–8, SPIE, 2004.
URL `http://link.aip.org/link/?PSI/5455/1/1`

[5] J.-L. A. Yeh, C.-Y. Hui, and C. Tien, "Electrostatic Model for an Asymmetric Combdrive". *IEEE J. Microelectromechanical Systems*, **9**(1):126–135, March 2000.

[6] W. C. Young, *Roark's Formulas for Stress & Strain*. McGraw-Hill, 6th edition, 1989, ISBN 0-07-100373-8.

[7] S. Timoshenko, *Théorie de l'élasticité*, pp. 265–271. Librairie polytechnique Ch. Béranger, Paris & Liège, 1936.

Chapter 3

Concept

In this chapter we develop the device concept for the two realized devices. First the optical application is presented which results in a number of constraints. The constraints and requirements yield the configuration of the device and the different device parameters are fixed. Finally the mechanical stability is investigated and the electro-mechanical behavior is predicted.

3.1 Tilting Platform Device

3.1.1 Motivation

In fiber optic telecommunications, wavelength-division multiplexing (WDM) is a technology used to multiplex several optical carrier signals on a single optical fiber by using different wavelengths (colors) of laser light to carry different signals. The WDM technology increases drastically the capacity of an optical fiber and hence reduces communication costs, but it also allows redirecting data traffic between different users and/or networks. WDM technology uses multiplexers to combine several carrier signals, and demultiplexers to separate

them. The multiplexing and demultiplexing of the carrier signals is achieved with optical filters. The optical filters are usually realized by cascading a number of individual single-frequency Fabry-Perot etalons having different lengths and thus resonating at different frequencies. The number of used Fabry-Perot etalons corresponds to the number of channels that can be (de-) multiplexed.

In contrast to filters based on cascaded etalons of fixed frequency, we want to realize a tunable filter based on the diffraction property of a grating. We used a so-called resonant grating filter (RGF) which in our case consists of three thin homogenous dielectric layers with a grating etched into the top most layer. This type of filter can exhibit an extremely narrow reflection spectral band (in our case $< 0.5\,\text{nm}$ FWHM) that otherwise would require a large number of uniform layers. The working principle of a reflection RGF is that a part of the incoming light is trapped through evanescent coupling into the waveguide. Destructive interference for the transmitted waves is obtained within a limited range of parameters, thus forming a resonance region. Outside this resonance region the light does not couple into the waveguide and is transmitted and reflected as from a regular stratified layer.

The wavelength of the reflected spectral band can be tuned by changing the angle of incidence of the RGF, i.e. by tilting the filter. For this purpose we need a device providing a tilting platform that can be electrically actuated and onto which the RGF can be assembled. The RGF is designed to work in a wavelength range from 1526 nm - 1573 nm (telecom C-band) with a tuning slope of $6\,\text{nm}/^\circ$. Hence the C-band can be tuned by mechanically tilting the filter by 8°. The RGF has been designed and fabricated in the context of another PhD thesis [1].

3.1.2 Constraints

In contrast to many RGF devices that work at normal incidence, the RGF used here is designed to work in oblique incidence at 45°. This choice makes it easier to separate the incident and the reflected

beams, but the advantage goes at the cost of a larger filter area. Whereas filters designed for normal incidence have a very high efficiency already for a small filter area [2], the oblique incidence filter used here has an efficiency which depends strongly on the grating area and on the spot size of the laser beam on the filter [3]. A trade-off between filter size and efficiency loss was found for a filter size of $2\times2\,\mathrm{mm}^2$ which reduces the maximum power efficiency to 64%, compared to a RGF with infinite surface.

3.1.3 Device Configuration

The fact that the filter efficiency depends among other factors on the spot size of the laser on the filter requires a suspension mechanism of the platform such that its gravity center does not perform

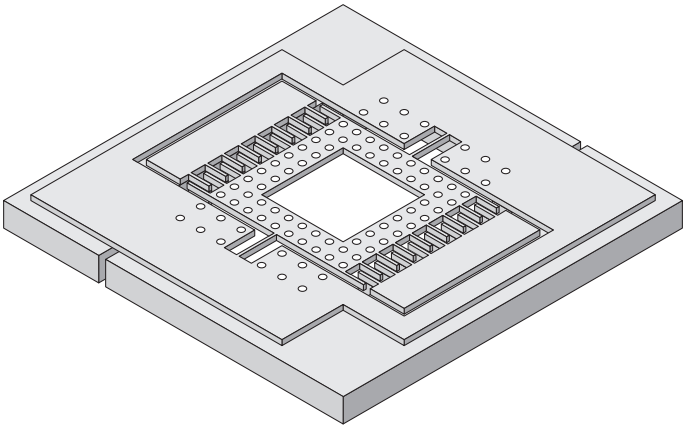

Figure 3.1: *Concept of the tilting platform device. The device layer contains the platform with the torsion beams and the mobile combs, as well as two static comb electrodes which are not used. The handle layer contains two backside static comb electrodes which are used for actuation.*

any vertical or lateral displacement when being tilted. Otherwise the illumination area and with it the filter efficiency would vary in function of the tilt angle. One possible configuration was found for a symmetrical suspension of the platform using two torsion beams. The suspension with two torsion beams provides one degree of freedom in the form of a pure tilt motion of the platform around the axis formed by the torsion beams. The required tilt range of 8° can then be achieved by tilting the platform by ±4°.

In order to tilt the platform a vertical force has to be applied at the edge of the platform. For this purpose we use vertically staggered comb actuators as discussed in Sec. 2.1.5. This type of actuator requires that the mobile and the static combs are vertically offset. The vertical offset between the mobile and the static combs can be realized by using so-called silicon-on-insulator (SOI) substrate and by structuring, respectively, the mobile combs in the device layer, and the static combs in the handle layer.

A model of the device is presented in Fig. 3.1. It shows the device layer which contains the quadratic platform of $2\times2\,\mathrm{mm}^2$ containing a hole of $1.6\times1.8\,\mathrm{mm}^2$ for optical transmission. The platform is attached with two torsion beams to a stable frame. The two re-

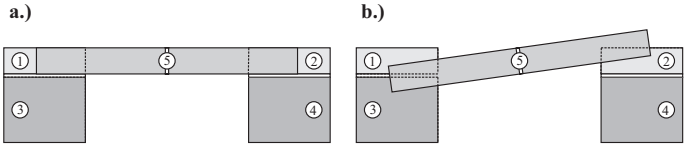

Figure 3.2: *Cross section showing the platform in its a) unactuated and b) in its actuated state. The mobile combs ⑤ and the static combs ① and ② are etched in the device layer, whereas the static combs ③ and ④ are etched in the handle layer of a SOI wafer. Device and handle layer are electrically isolated by a buried oxide layer. A voltage between the combs ③ and ⑤ results in a vertical force pulling down the platform at the left side (b).*

maining edges of the platform are equipped with the mobile combs that are part of the vertically staggered comb actuator. Moreover, two static combs are provided in the device layer. They have been foreseen for capacitive measurement of the tilt position, an idea that has been abandoned later. The handle layer contains a large recess area underneath the platform, and two static comb electrodes used for actuation. The static combs in the handle layer have the same footprint than the static combs in the device layer.

The arrangement of the different comb electrodes is illustrated in Fig. 3.2. A total of five comb electrodes are provided on two levels, and all five electrodes are electrically isolated from each other. Electrode number ⑤ represents the mobile combs which are attached to the platform. The electrodes number ① and ② represent the top static combs, while the electrodes number ③ and ④ represent the bottom static combs. With this arrangement a vertical stack is formed between the bottom static electrodes ③ and ④, and the top static electrodes ① and ② and the mobile electrode ⑤, respectively. By applying a potential difference between the mobile electrode ⑤ and the bottom static electrode ③, a vertical force is created, pulling down the platform on the left side resulting in a tilt motion due to the symmetrical suspension. Similarly, the platform tilts to the right side for a potential difference applied between the electrodes ⑤ and ④. The top static comb electrodes number ① and ② are not used for actuation.

3.1.4 Device Modeling

A. Choice of SOI Substrate

The thickness of the device layer of the SOI substrate has to be chosen in function of the size of the platform and the required tilt angle. The tilt angle θ is associated to a vertical displacement z at the extremity of the mobile combs according to

$$z = (R + r) \cdot \tan\theta \tag{3.1}$$

where R is half the width of the platform (see Fig. 2.5), and r is the length of the attached mobile combs. With a platform size of $2\times2\,\mathrm{mm}^2$ ($R = 1000\,\mu\mathrm{m}$), a comb length of $r = 100\,\mu\mathrm{m}$, and a maximum tilt angle of $\theta_{max} = \pm4°$, the vertical displacement yields $z = 75\,\mu\mathrm{m}$, which is then the required thickness of the device layer. In the case where the vertical displacement z exceeds the device layer thickness, the calculus of the position dependent capacity of the engaged combs in Eq. 2.28 is not correct anymore.

The choice of the thickness of the buried silicon dioxide (SiO_2) layer is a compromise between tolerable stress induced in the substrate, electrical drift due to trapped charges in the dielectric, and dielectric breakdown voltage. According to Shea *et al.*, the dielectric breakdown voltage for an electrode gap of less than approximately $2\,\mu\mathrm{m}$ decreases linearly to zero with the gap spacing, reflecting the increasing field emission current at smaller gaps [4]. For this reason a thick layer of buried SiO_2 would be an advantage, but on the other side the compressive nature of SiO_2 induces stress which can result in bow of the SOI substrate. Therefore, we decided to use SOI wafers with a thickness of the buried SiO_2 of $2\,\mu\mathrm{m}$.

The thickness of the handle layer has no direct impact on the device. It needs just to be thicker than the device layer in order to prevent the mobile combs in the actuated state from touching the carrier substrate onto which the chips will be wire bonded. At the time when this PhD thesis was started, the thinnest available handle layer thickness for SOI wafers was $350\,\mu\mathrm{m}$.

B. Width and Gap of the Combs

In DRIE, the etch rate depends strongly on the size of the etched structures, i.e. small features etch much slower than large openings. This leads to the phenomenon of underetching of large structures. Hence, best results in terms of etch homogeneity and verticality of the etched structures are achieved when the etched feature sizes are identical all over the wafer. This is especially true when etching very thick substrates. We therefore designed the device such that all the

trenches in the handle layer have exactly the same size. Different tests showed that the width of the trenches in the 350 µm thick handle layer should be at least 20 µm to ensure a good verticality of the sidewalls. Vertical sidewalls are required for the combs in order to minimize parasitic electrostatic effects. In accordance with these considerations, we made two different designs where the trenches separating the combs in the handle layer have a width of 20 µm and 30 µm, respectively. The width of the static combs, w_{sc}, was fixed to the same values, i.e. 20 µm and 30 µm.

The dimensions of the static and the mobile combs in the device layer and their arrangement with respect to the static combs in the handle layer is illustrated in Fig. 3.3. The static combs in the device layer have the same width and the same position like the static combs in the handle layer. The mobile combs of width w_{mc} are symmetrically arranged between two adjacent static combs, i.e.

$$w_{mc} + 2 \cdot g = w_{sc} \tag{3.2}$$

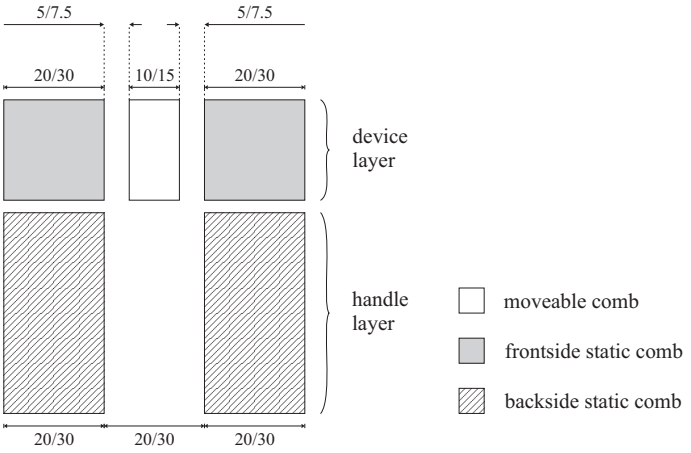

Figure 3.3: *Arrangement and dimensions of the different combs in the device and in the handle layer. Units are in µm.*

For the two different designs, the width of the mobile combs was fixed to 10 µm and 15 µm, resulting in a gap between the mobile and the static comb of 5 µm and 7.5 µm.

C. Total Number of Combs

The number N of mobile combs that can be arranged along the edge length L of the platform calculates according to

$$L = N \cdot w_{mc} + (N+1) \cdot w_{sc} + 2N \cdot g \tag{3.3}$$

where w_{mc} is the width of the mobile combs, w_{sc} is the width of the static combs, and g designates the gap between mobile and static combs. Solving Eq. 3.3 for N and using the relation in Eq. 3.2 yields the number N of mobile combs:

$$N = \frac{1}{2}\left(\frac{L}{w_{mc} + 2g} - 1\right) \tag{3.4}$$

In the case of a platform edge length of $L = 2000\,\mu\text{m}$, Eq. 3.4 yields $N = 33$ mobile combs of width $w_{mc} = 15\,\mu\text{m}$, and $N = 49$ mobile combs of width $w_{mc} = 10\,\mu\text{m}$.

		Design 1	Design 2
Static Comb Width	w_{sc}	20	30
Mobile Comb Width	w_{mc}	10	15
Gap	g	5	7.5
Comb Length	r	200	300
Number of Combs	N	49	33
Platform Length	L	2010	2010
Half Platform Width	R	1000	1000
Maximum Tilt Angle	θ_{max}	4	4

Table 3.1: *Summary of the fixed parameters. Units are in µm for lengths, and deg. for tilt angle.*

D. Evaluation of Torsion Beam Width and Length

In order to evaluate the required dimensions of the torsion beams, we have to analyze the electro-mechanical system in its maximum actuated position, i.e. for a tilt angle of $\theta = 4°$. According to Sec. 2.3, the potential energy of the mechanically deformed torsion beams equals the electrostatic energy of the comb actuators:

$$U_M - U_E = 0 \tag{3.5}$$

Using Eq. 2.34 for the potential energy U_M of the torsion beams with the spring constant derived in Eq. 2.36, and using Eq. 2.8 for the electrostatic energy U_E with the capacity of a unit comb calculated in Eq. 2.28, the explicit form of the energy equilibrium condition writes

$$\frac{Ghw^3}{3l}\left(1 - \frac{192}{\pi^5}\frac{w}{h}\right)\theta - \epsilon_0\epsilon_r\frac{2Rr + r^2}{g}NV^2 = 0 \tag{3.6}$$

The height of the torsion beams is defined by the thickness of the device layer (75 µm). The width and the length of the torsion beams have to be fixed in function of the desired electro-mechanical properties. For this purpose the actuation voltage V for which the maximum tilt angle of $\theta = 4°$ is achieved was arbitrarily set to $V = 90\,\mathrm{V}$. This choice was motivated by the fact that a (desirable) lower actuation voltage would require more flexible torsion beams that are unfavorable in terms of device stability.

So far, the only parameters in Eq. 3.6 that are not yet determined are the length l and the width w of the torsion beams. The parameter space of l and w for constant torque can be graphically presented by solving Eq. 3.6 for l and plotting l as a function of w:

$$l = \frac{1}{3}\,\frac{Ghw^3}{2Rr + r^2}\left(1 - \frac{192}{\pi^5}\frac{w}{h}\right)\frac{g}{\epsilon_0\epsilon_r}\frac{\theta}{NV^2} \tag{3.7}$$

The corresponding plots for the two different comb configurations according to Tab. 3.1 are presented in Fig. 3.4. The figure reveals also that the two comb configurations are chosen such that the

electro-mechanical characteristic is almost identical. The choice for the appropriate ratio of torsion beam length vs. width in Fig. 3.4 is conducted by concerns about fabrication tolerances on the dimensions of the torsion beams. Vertical structures etched by DRIE have typically a negative sidewall angle of 0.5° to 1.5°. With respect to the 75 µm high torsion beams, this means that the torsion beams may be up to 4 µm thinner at the bottom than at top. Therefore we fixed the width of the torsion beams to $w = 8\,\mu m$ and the length to $l = 680\,\mu m$. In the case where the torsion beams should turn out to be too rigid, the width could still be reduced by oxidation and oxide removal.

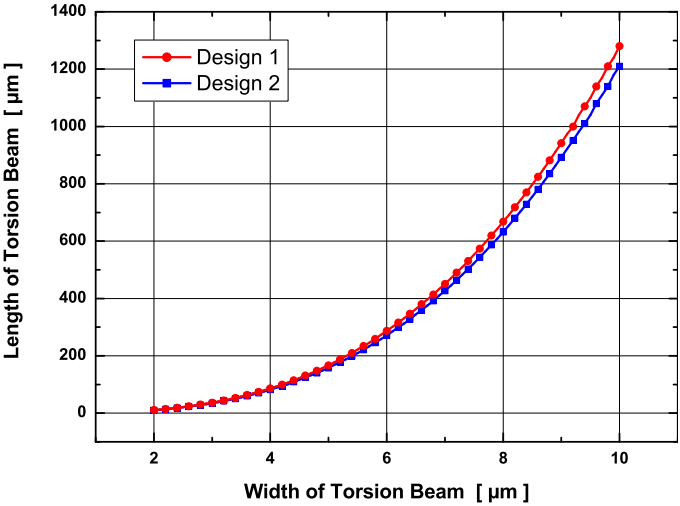

Figure 3.4: *Ratio of length vs. width of a torsion beam, evaluated at a tilt angle of $\theta = 4°$ and an actuation voltage of $V = 90$ V. The modulus of rigidity G was calculated for isotropic material with an elastic modulus of $E = 165$ GPa.*

3.1.5 Prediction of the Device's Characteristics

In order to evaluate the tilt angle in function of the applied actuation voltage, we solve Eq. 3.6 of the energy equilibrium condition for θ:

$$\theta = \frac{\epsilon_0 \epsilon_r (2Rr + r^2)}{g} \frac{3l}{Ghw^3} \left(\frac{1}{1 - \frac{192}{\pi^5} \frac{w}{h}} \right) NV^2 \tag{3.8}$$

The tilt angle θ in Eq. 3.8 scales linearly with the length l and the height h of the torsion beam, but to the power of three with its width w. The length and the width of the torsion beams are defined by the microfabrication process and are subject to fabrication tolerances related to a mismatch of process parameters in photolithography (exposure dose, development time) and DRIE (underetching). The fabrication tolerances are absolute errors that are typically in the range of $\pm 0.5\,\mu m$. Due to the huge ratio of beam length to beam width, the relative impact of fabrication tolerances onto the length is negligible, while it is quite important for the width.

Based on Eq. 3.8, we established the expected angle-voltage characteristic which is depicted in Fig. 3.5. We also evaluated the influence of $\pm 0.5\,\mu m$ fabrication tolerances. The quite strong impact on the beam width is partially compensated by the changing gap distance. The parameters used in Eq. 3.8 are summarized in Tab. 3.2.

Half Platform Width	R	1000	µm
Number of Combs	N	33	
Comb Length	r	300	µm
Gap	g	7.5 ∓ 0.5	µm
Beam Width	w	8.0 ± 0.5	µm
Beam Length	l	680	µm
Beam Height	h	75	µm
Modulus of Rigidity	G	105	GPa

Table 3.2: *Parameters used in Eq. 3.8 to plot the graphs in Fig. 3.5.*

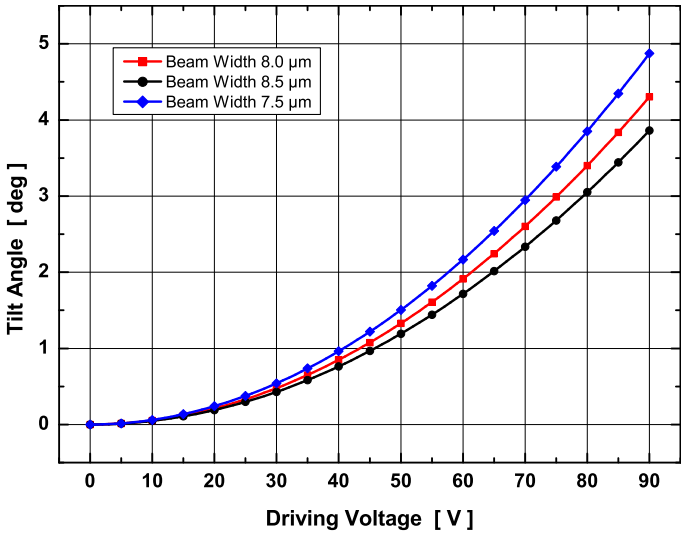

Figure 3.5: *Influence of fabrication tolerances on the voltage-angle characteristics. The huge impact of beam width variation is partially compensated by the variation of the gap between the combs.*

3.1.6 Influence of Beam-Shape on Stability

A. Stability Problem

The in-plane stability of a symmetrically suspended mirror using two opposite torsion beams is a known issue of scanning mirror devices [5]. Instead of a tilt motion around the axis formed by the two torsion beams, the mirror often performs a parasitic in-plane rotation around the symmetry axis normal to the mirror plate. There are various reasons for this problem.

One reason refers to the lateral misalignment between mobile and static combs. Already a small offset error creates an in-plane force perpendicular to the combs. In static operation where only

the comb actuators on one side of the platform are used for tilting, the misalignment results directly in rotation of the platform due to pull-in. Since the combs are attached at the extremity of the platform, the rotation angle at which the mobile and static combs get in contact is as small as 5 mrad. In dynamic operation the in-plane rotation about the central axis of the platform can not be avoided neither since the motion corresponds to a higher order mode being easily excited.

Another reason for the parasitic in-plane rotation of the platform can be attributed to process-induced stress in the SOI substrate [6] which results in buckling of the torsion beams [7].

An interesting approach to reduce parasitic in-plane rotation has been proposed by Tsuboi *et al.* [8] who replaced the straight torsion beam by a V-shaped torsion beam. The V-shape of their torsion beam provides lateral stability, but the required torque for a given tilt angle increases as well.

B. Hourglass-Shaped Torsion Beam

In the context of the problems encountered with torsion beams in terms of instability and buckling at high actuation voltages, different shapes of torsion beams have been investigated. One of the shapes analyzed in detail has the shape of an hourglass, as depicted in

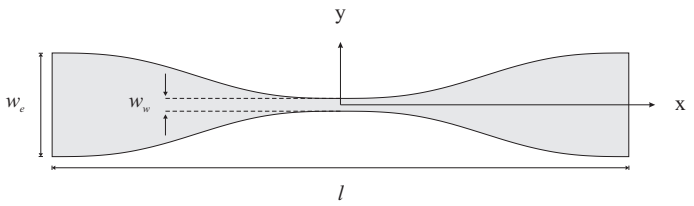

Figure 3.6: *A torsion beam with the shape of an hourglass improves considerably the lateral stability.*

Fig. 3.6. Its upper and lower two legs are described by

$$\begin{aligned} y_u &= +\frac{w_w}{2} \mp \frac{w_e - w_w}{l} \cdot x \pm \frac{w_e - w_w}{4\pi} \cdot \sin\left(\frac{4\pi}{l}x\right), \\ y_l &= -\frac{w_w}{2} \pm \frac{w_e - w_w}{l} \cdot x \mp \frac{w_e - w_w}{4\pi} \cdot \sin\left(\frac{4\pi}{l}x\right), \end{aligned} \tag{3.9}$$

in the interval $-\frac{l}{2} < x < \frac{l}{2}$. The parameters w_w, w_e, and l designate the width at the waist of the beam, the width at the end of the beam, and the length of the beam. The function described by Eq. 3.9 is characterized by continuous differentiability, which contributes to a very smooth stress distribution along the torsion beam. This is of particular interest since crystalline structures always break at points where stress is accumulated.

C. Comparison of Stability

We performed a series of ANSYS FEM simulations to compare the lateral stability of a platform that was once suspended by hourglass-shaped torsion beams, and once by regular straight beams. The stability evaluation was also carried out with respect to undercut of the two torsion beams. Undercut is a phenomenon related to DRIE where the etched structures are often thinner at the bottom than at top. As a result, the original rectangular cross section of a torsion beam appears rather to be trapezoidal.

Beam Shape	Straight	Hourglass
length l [µm]	680	680
height h [µm]	75	75
width w [µm]	8.5	
width at waist w_w [µm]		6
width at end w_e [µm]		16

Table 3.3: *The dimensions of the simulated regular straight torsion beam and the hourglass-shaped torsion beam.*

The exact dimensions of the two investigated beams are summarized in Tab. 3.3. The two beams had the same length and the same height. The width was chosen such that the resulting torque of the two beams was identical in the case where the beams did not suffer from undercut. The corresponding plot of vertical displacement Δz in function of applied force F_z is given, respectively, by the continuous blue and red graph in Fig. 3.7. For undercut angles of $1\,^\circ$ and $2\,^\circ$, the resulting vertical displacement Δz increases for both types of torsion beams, but the increase is more pronounced for hourglass-shaped torsion beams. This is an advantage since the

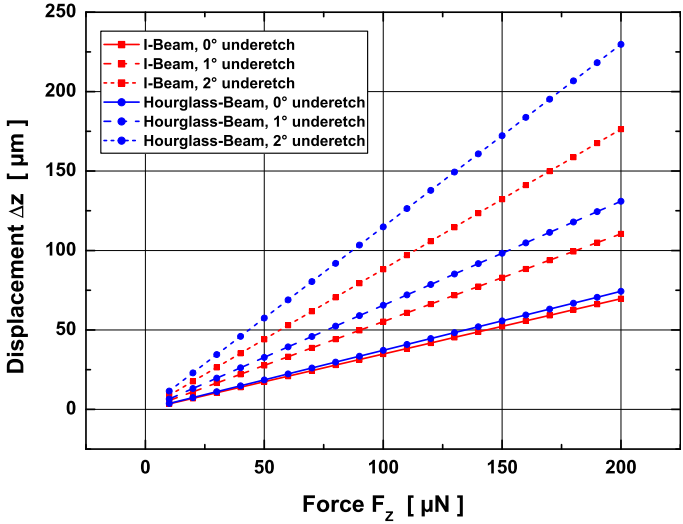

Figure 3.7: *Vertical force F_z applied onto the platform edge and resulting displacement Δz of the platform edge for the two cases where the platform is suspended with straight torsion beams and hourglass-shaped torsion beams, respectively. The dimensions of the torsion beams are chosen such that the vertical displacement is identical in the case without undercut.*

required torque can then be achieved with a lower actuation voltage which reduces also the risk of pull-in.

In order to analyze the influence of misalignment between the mobile and static combs, we simulated the lateral displacement Δx as a result of a lateral force F_x applied at the edge of the platform. According to Fig. 3.8, a lateral force of 100 µN results in a displacement Δx of 1.2 µm in the case where the platform is suspended using straight beams that are not affected by undercut. Under the same conditions, the lateral displacement Δx using hourglass-shaped torsion beams was only 0.38 µm which corresponds to a reduction

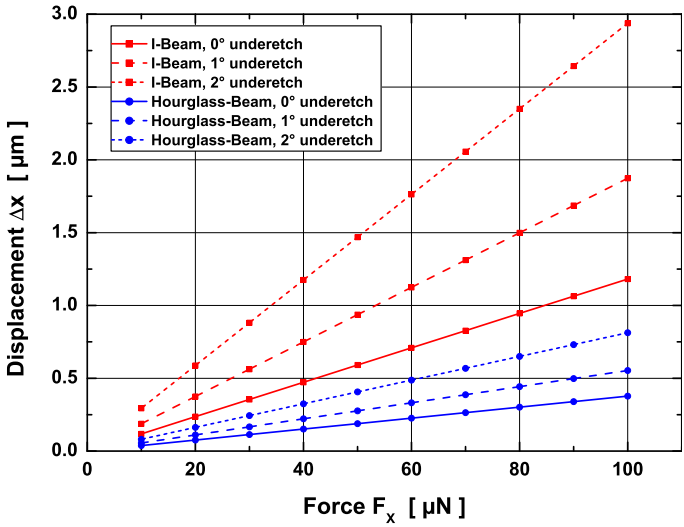

Figure 3.8: *A lateral force F_x is applied at the edge of the platform in order to study the influence of comb misalignment resulting in lateral displacement Δx and electrostatic pull-in. The graph shows that the use of hourglass-shaped torsion beams rather than straight torsion beams yields in a better lateral stability, and the influence of undercut is reduced.*

of 68%. For undercut angles of 1 ° and 2 °, the resulting lateral displacement Δx increases for both types of torsion beams, but the hourglass-shaped torsion beams are much less affected than the straight torsion beams. The use of hourglass-shaped torsion beams instead of straight torsion beams increased the lateral stability by 70% for an undercut angle of 1 °, and by 72% for an undercut angle of 2 °.

D. Conclusion

The use of hourglass-shaped torsion beams can not avoid parasitic in-plane rotation of the platform, but it increases considerably the lateral stability. In the case of undercut of the beams, the lateral stability of hourglass-shaped torsion beams is much less affected than that of straight torsion beams. On the other hand, the reduction of the required torque due to undercut is more important for hourglass-shaped torsion beams than for straight torsion beams. Overall, the use of hourglass-shaped torsion beams increases the voltage at which the device gets instable, and thus the stable range of the device is extended.

3.2 Piston Tip-Tilt Mirror Device

3.2.1 Motivation

Many applications in optics require very flat and accurately displaceable micromirrors. Typical devices are tunable cavity systems such as interferometers, lasers, and filters. In these applications MEMS devices are often used.

Recent optical MEMS developments have shown that silicon-on-insulator (SOI) based devices are superior to poly-silicon structures in terms of flatness and surface deformation especially when operating devices in resonance [9]. However, SOI devices are subject to bow due to process-induced stress in the SOI substrate [6]. Additional mechanical stress can be introduced to the device by packaging and thermal mismatch effects.

In the context of the stated problem we wanted to develop a piston tip-tilt mirror device providing an optically flat mirror and accurate displacements using asymmetric vertical comb drives.

3.2.2 Device Concept

In order to achieve an optically flat mirror, a suspension concept was sought that compensates residual stress present in the device. Since comb drives are prone to lateral snap-in when used in static mode, the suspension had to provide high lateral stiffness combined with high vertical flexibility for actuation purpose.

One of the solutions found is presented in Fig. 3.9. The triangular mirror is suspended by three C-shaped beams which are folded around the mirror and the actuators. The C-shape of the beams contributes to a very compact device despite the length of the beams. The length of the beams provides the required flexibility for vertical actuation, while the shape and the arrangement of the beams reduce undesired lateral displacement like in-plane rotation. The vertical flexibility is further increased by reducing the height of the suspension beams over the height of the device. The proposed suspension

concept allows the mirror to perform a vertical motion as well as a small tip-tilt which can be useful to correct a wedge error with another optical component. Unlike the torsion beams in a scanning mirror device which form a straight axis where stress can propagate and cause buckling of the torsion beams [7], the suspension with three C-shaped beams arranged in 120 ° segments avoids stress propagation and buckling of the beams. Instead, residual stress in the SOI substrate outside the mirror zone results in a small lateral deformation of the beams which occurs mainly in the flat part of the beam. The particular shape of the beams is based on a sine function characterized by continuous differentiability all along the beam, which yields in a very smooth stress distribution during actuation.

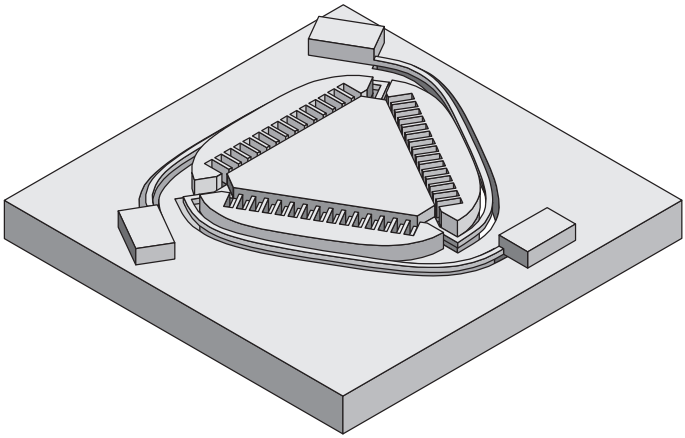

Figure 3.9: *Concept drawing of the piston tip-tilt mirror device. The device provides a triangular mirror with an edge length of 1.7 mm. The mirror is symmetrically suspended by three C-shaped beams. Three sets of asymmetric vertical comb actuators allow the mirror to be actuated either in a pure piston mode, or in a piston mode with an additional tip-tilt.*

For actuation we use asymmetric vertical comb actuators. In this type of actuator the height of the mobile combs is reduced over the height of the static combs such that the mobile and the static combs are vertically offset in the initial position. When applying a potential to the static combs with respect to the mobile combs, a vertical force is created in the inhomogeneous electric field between the offset combs which lifts up the mobile combs and the attached mirror. In total three static comb electrodes are provided. Pure vertical displacement is achieved when the same voltage is applied on all three static comb electrodes. When applying different voltages to the three static comb electrodes, the mirror performs a tip-tilt.

3.2.3 Device Modeling

A. Mirror Size

The size of the equilateral triangular mirror is defined by an inscribed circle of radius r_m that touches the three edges of the triangle. The corresponding edge length L of the triangular mirror calculates according to

$$L = \frac{2\, r_m}{\tan(30°)} \tag{3.10}$$

In order to avoid beam clipping when experimenting with a laser, we set $r_m = 500\,\mu\text{m}$ which yields a reasonable size for the mirror. The edge length of the mirror is then $L = 1732\,\mu\text{m}$.

B. Comb Actuators

The number N of combs that can be arranged along the edge length L of the triangular mirror calculates according to

$$L = N \cdot w_{mc} + (N+1) \cdot w_{sc} + 2N \cdot g \tag{3.11}$$

where w_{mc} is the width of the mobile combs, w_{sc} is the width of the static combs, and g designates the gap between mobile and static

combs. The three realized designs and the corresponding values for the different comb parameters are summarized in Tab. 3.4.

C. Suspension Beams

The C-shaped suspension beam is composed of two identical segments where the first segment is defined by

$$y_c = \frac{H_y}{H_x}x - \frac{H_y}{\pi}\sin\left(\frac{\pi}{H_x}x\right),\ x \leq H_x, \tag{3.12}$$

and the second segment is obtained by mirroring the segment y_c at the normal y_n in point $x = H_x$. The corresponding drawing is depicted in Fig. 3.10. The function describing the segments of the C-shaped beam has the property of continuous differentiability and infinite radius of curvature at the two end points. This characteristic contributes to a very smooth stress distribution along the beam, avoiding stress concentration and potential breaking of the beams under load. The total curvature of the C-shaped beam was fixed at 120 °. This choice allows to arrange the three C-shaped beams with their flat region parallel to the edges of the triangular mirror, resulting in the most compact configuration. According to Fig. 3.10, the angle of curvature of the segment y_c described by Eq. 3.12 can be

L	h_{sc}	h_{mc}	w_{sc}	w_{mc}	g	N
1463	50	12	7	7	7	52
1465	50	12	5	5	5	73
1480	50	12	10	10	5	49

Table 3.4: *Parameters for the three different comb actuator designs. L : edge length of triangular mirror; h_{sc} : height of static combs; h_{mc} : height of mobile combs; w_{sc} : width of static combs; w_{mc} : width of mobile combs; g : gap; N : number of mobile combs per edge. The units of the parameters designating dimensions are micrometers.*

calculated by equalizing its derivative y_c' at $x = H_x$ with the desired slope ϕ:

$$y_c'(H_x) = \tan(\phi) \tag{3.13}$$

Solving Eq. 3.13 for $\phi = 60\,^\circ$ yields the required ratio between the parameters H_x and H_y for the desired angle of curvature:

$$H_y = \frac{\sqrt{3}}{2} H_x \tag{3.14}$$

Hence, the segment y_c with the desired angle of curvature of $60\,^\circ$ is

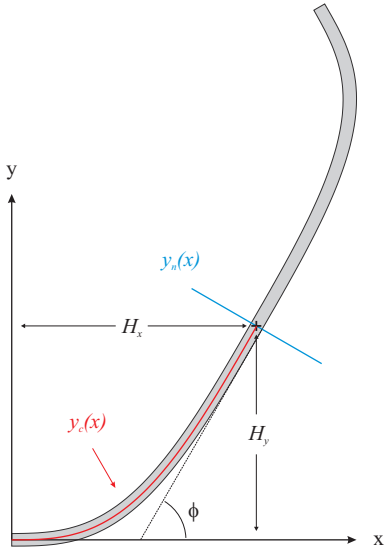

Figure 3.10: *The C-shaped suspension beam is composed of two segments, where the first segment (red graph) is defined by the function $y_c(x)$ in Eq. 3.12, and the second segment is obtained by mirroring the first segment at the normal $y_n(x)$.*

given by

$$y_c = \frac{\sqrt{3}}{2}x - \frac{\sqrt{3}H_x}{2\pi}\sin\left(\frac{\pi}{H_x}x\right),\ x \leq H_x. \tag{3.15}$$

The size of the segment y_c depends on the scaling parameter H_x which has to be chosen in function of the mirror size. We fixed this parameter to $H_x = 1000\,\mu\text{m}$.

The total length l_c of the C-shaped suspension beam calculates according to

$$l_c = 2\int_0^{H_x} \sqrt{1 + y_c'(x)^2}\,dx \tag{3.16}$$

where the factor of 2 takes into account that the beam is composed of two segments $y_c(x)$. With $H_x = 1000\,\mu\text{m}$, Eq. 3.16 yields a length of $l_c = 2820\,\mu\text{m}$.

The rectangular cross section of the beams has an aspect ratio of beam height vs. beam width of 1:2 - 1:3. This choice ensures a better lateral stability and at the same time a better flexibility for vertical actuation. The height of the suspension beam h_b is reduced during the fabrication process to a value of approximately $12\,\mu\text{m}$. The width w_c of the suspension beam was fixed to $w_c = 30\,\mu\text{m}$.

3.2.4 Mechanical Properties of the Beams

A. Restoring Force

We have calculated the restoring force of the C-shaped suspension beam using an analytically approximated model, and we have compared the results to the ones obtained by FEM simulations. The analytically approximated model is based on the deflection theory introduced in Sec. 2.2.2. In this model we did not consider the effect of torsional deformation which occurs due to the curved shape of the beams. However, the additional torsional restoring force is expected

to be rather small due to the huge ratio of beam length to vertical displacement. Using the length l_c given by Eq. 3.16, and taking into account that the mirror is suspended by three suspension beams, the total mechanical restoring force $F_{M_{tot}}$ based on the calculus in Sec. 2.2.2 writes

$$F_{M_{tot}} = -3\,E\frac{w_c\,{h_c}^3}{{l_c}^3}\cdot z \tag{3.17}$$

Fig. 3.11 represents the restoring force vs. vertical displacement of the mirror. The graph entitled "Analytical" is based on Eq. 3.17, while the graph entitled "ANSYS" is based on FEM simulations using

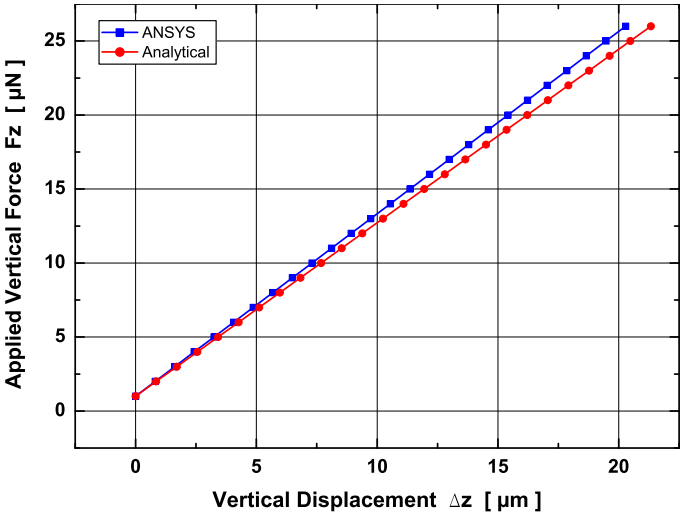

Figure 3.11: *Analytical approximation and FEM simulation of the vertical displacement of the mirror under load. The approximated model neglects torsional stiffness resulting from the deflection of a curved beam. Hence, the beam appears less stiff and yields an increased vertical displacement of 5%.*

ANSYS. The simulation results were obtained by applying a vertical force to the center of the mirror and evaluating the displacement. The difference of 5% between the two graphs can be explained by the neglected effect of torsional deformation which results in a lower restoring force in the analytical approximation.

B. Lateral Stability

The lateral stability of the proposed suspension mechanism was analyzed using ANSYS finite element modeling. For this purpose a load with a vector in the xy-plane (mirror plane) was applied at three different positions on the triangular mirror, as indicated in Fig. 3.12. The resulting displacement and stress values are summarized in Tab. 3.5. The maximum lateral displacement was evaluated to be 1 µm for a load of 50 µN. In contrast, a vertical force of 25 µN applied in the center of the mirror resulted in a vertical displacement of 20 µm. It can be concluded that the suspension with 3 C-shaped beams is 40 times stiffer in the xy-plane than in z-direction. The high stiffness in the xy-plane shows that an eventual misalignment between static and mobile combs and the resulting in-plane force

	Force		Displacement			Stress
Direction	Value	Position	UX	UY	UZ	S1
FZ	25	3	1.0	0.1	43.7	34.0
FZ	25	2	0.1	0.1	20.3	18.0
FZ	25	1	0.5	0.1	27.0	28.7
FY	50	3	0.5	1.0	0.5	9.0
FX	50	3	0.5	0.5	0.5	8.5
FY	50	1	1.0	1.0	0.1	13.5

Table 3.5: *The columns indicate the direction of applied force, force amount, and the location on the mirror where the force was applied to, respectively, as well as the displacements and the maximum first principal stress. Units are in µMKS.*

between the combs yields only a small lateral displacement. The very low first principal stress values of 18 MPa at 20 µm vertical displacement confirms the assumption that the additional torsional stiffness caused by the deflection of curved beam is quite low in our case.

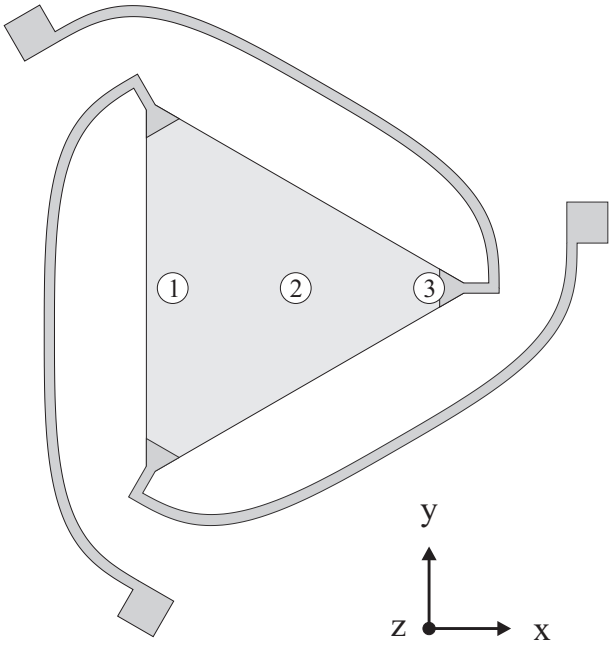

Figure 3.12: *Model for the analysis of the lateral stability. Different forces with force vectors in x-, y-, and z-direction were applied at the numbered locations, and the corresponding displacement was evaluated using FEM simulation.*

3.2.5 Evaluation of Electrostatic Force

The electrostatic force in the inhomogeneous electric field between the vertically offset combs of different height was evaluated by FEM simulation using CoventorWare. For this purpose we established a model of a unit comb drive, as depicted in Fig. 3.13. It consists of a U-shaped static comb and an interdigitated mobile comb of reduced height. We studied the two cases where once an additional grounded substrate was provided underneath the combs, and once not. The purpose of the additional grounded substrate is to shield the mobile combs from fringing electric fields at the bottom.

In order to evaluate the attainable electrostatic force, we set the mobile combs to different vertical positions with respect to the static combs and evaluated by FEM analysis each time the position dependent capacity. The corresponding force was then calculated according to

$$F_E = -\frac{1}{2}\frac{\partial C}{\partial z} N V^2 \tag{3.18}$$

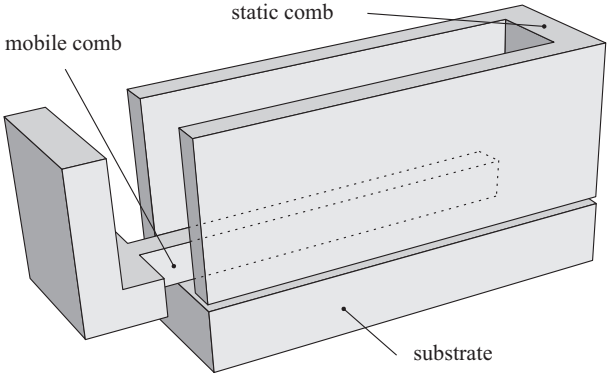

Figure 3.13: *Model of the unit asymmetric vertical comb actuator used for the simulation with CoventorWare.*

The resulting plots of the position dependent electrostatic force are depicted in Fig. 3.14. The plots are based on an actuation voltage of 1 V and refer to the device having a total of 3×52 combs separated by a gap of 7 µm. The FEM simulation shows that the available electrostatic force can be significantly increased in the case where a grounded substrate is provided underneath the combs. Since MEMS devices are typically operated by providing a supply voltage to the static combs while the mobile combs are grounded, the presence of a grounded substrate shields the mobile combs from the fringing fields at the bottom edge, and the resulting upward force increases.

According to Fig. 3.14, the upward electrostatic force decreases

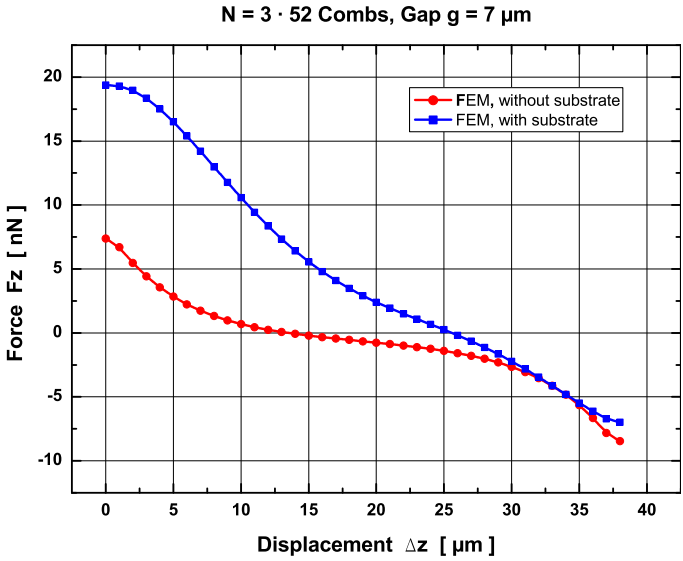

Figure 3.14: *FEM simulation of the electrostatic force achieved at 1 V. The simulation reveals that the presence of a grounded substrate underneath the combs significantly increases the electrostatic force.*

the more the mobile combs are lifted up. For a given displacement of the mobile combs, the upward and downward vertical force acting on the top and the bottom of the mobile combs cancel each other out, and the resulting force is zero. Beyond this position, the downward electrostatic force becomes dominant. The position where the upward and downward forces cancel each other out is reached at 25 µm in the case where a grounded substrate is provided, and at 13 µm in the case without grounded substrate. The graphs to the right side of the force reversal point are irrelevant since the force has the same direction than the restoring force of the suspension beams.

A complete force versus displacement diagram as a function of different voltages is obtained by multiplying the graphs in Fig. 3.14

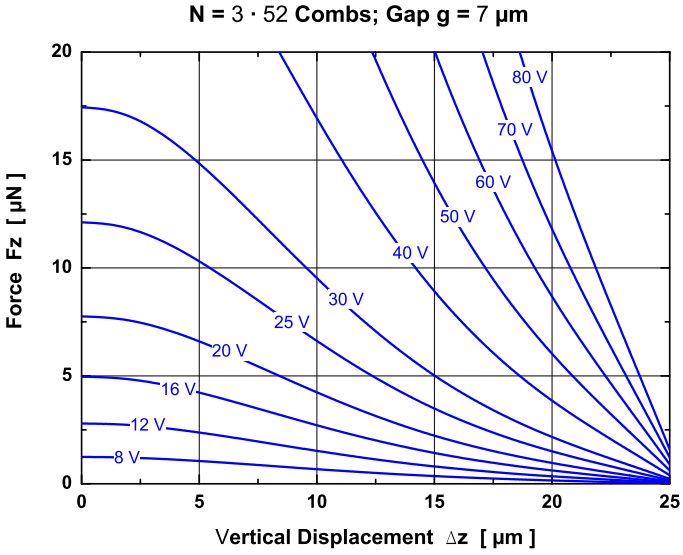

Figure 3.15: *Force diagram as a function of displacement and applied voltage. The plot was obtained by multiplying the blue graph in Fig. 3.14 with the indicated squared voltage values.*

with the squared voltage values. The corresponding diagram for the blue graph representing a device with grounded substrate underneath the combs is shown in Fig. 3.15.

3.2.6 Prediction of the Device's Characteristics

In order to predict the vertical displacement of the mirror vs. the applied voltage, we superimposed the plot of the electrostatic force diagram of Fig. 3.15 with the plot of the mechanical deflection vs. the restoring force, depicted in Fig. 3.11. The result is represented in Fig. 3.16. Then, we plotted the displacement values at the in-

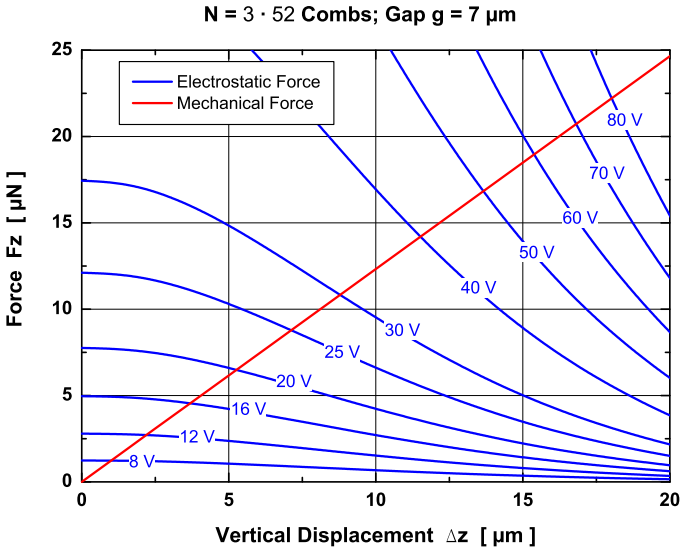

Figure 3.16: *Superposition of the electrostatic force diagram of Fig. 3.15 with the mechanical restoring force of Fig. 3.11. The intersections indicate the achieved displacement / force for a given supply voltage.*

tersections of restoring force and electrostatic force against the corresponding voltage values. We repeated this operation for the two cases where once a grounded substrate is provided underneath the comb actuator and once not, and for the two different comb configurations, i.e. for the device with 3×73 combs and a gap of $g = 5\,\mu\text{m}$, and for the device with 3×52 combs and a gap of $g = 7\,\mu\text{m}$. The results are depicted in Fig. 3.17. One can see that the presence of a grounded substrate underneath the comb actuator results in an increase of the vertical displacement by a factor of two. Very interesting is also the fact that both comb configurations have more or

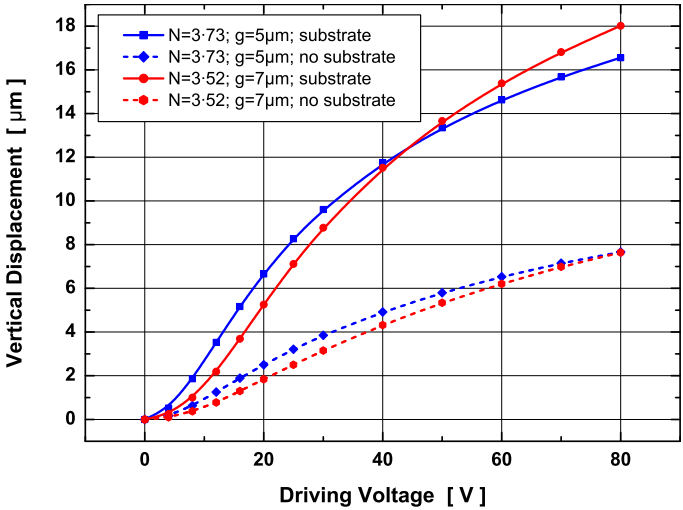

Figure 3.17: *FEM simulation of displacement vs. applied voltage. Very interesting is the large levitation effect of a grounded substrate underneath the comb actuator, which doubles approximatively the attainable displacement. Another interesting result is the fact that the device with smaller gaps and more combs does not achieve a larger displacement.*

less the same displacement characteristic although in one configuration 40% more combs are provided and at the same time the gap is reduced from 7 µm to 5 µm resulting in an even higher electric field.

Bibliography

[1] G. Niederer, *Resonant Grating Filters for Microsystems*. Ph.D. thesis, University of Neuchâtel, Switzerland, 2004.

[2] E. Bonnet, A. Cachard, A. V. Tishchenko, and O. M. Parriaux, "Scaling rules for the design of a narrow-band grating filter at the focus of a free-space beam". In "Photonic Crystal Materials and Nanostructures", volume 5450, pp. 217–222, SPIE, 2004. URL `http://link.aip.org/link/?PSI/5450/217/1`

[3] G. Niederer, H. P. Herzig, J. Shamir, H. Thiele, M. Schnieper, and C. Zschokke, "Tunable, oblique incidence resonant grating filter for telecommunications". *APPLIED OPTICS*, **43**(8):1683–1694, March 2004.

[4] H. R. Shea, A. Gasparyan, H. B. Chan, S. Arney, R. E. Frahm, D. López, S. Jin, and R. P. McConnell, "Effects of Electrical Leakage Currents on MEMS Reliability and Performance". *IEEE Transactions on Device and Materials Reliability*, **4**(2):198–207, June 2004.

[5] H. Schenk, *Ein neuartiger Mikroaktor zur ein- und zweidimensionalen Ablenkung von Licht*. Ph.D. thesis, Gerhard-Mercator-Universität-Gesamthochschule-Duisburg, 2000.

[6] A. Tiberj, B. Fraisse, C. Blanc, S. Contreras, and J. Camassel, "Process-induced strain in silicon-on-insulator materials". *Journal of Physics: Condensed Matter*, **14**(48):13411–13416, March 2002.
URL `http://stacks.iop.org/0953-8984/14/13411`

[7] K. Isamoto, K. Kato, A. Morosawa, C. Chong, H. Fujita, and H. Toshiyoshi, "A 5-V Operated MEMS Variable Optical Attenuator by SOI Bulk Micromachining". *IEEE J. Select. Topics Quantum Electron.*, **10**(3):570–578, May/June 2004.

[8] O. Tsuboi, Y. Mizuno, N. Koma, H. Soneda, H. Okuda, S. Ueda, I. Sawaki, and F. Yamagishi, "A Rotational Combdriven Micromirror with a Large Deflection Angle and Low Drive Voltage". In "Digest of the 15th IEEE Int. Conf. on Micro Electro Mechanical Systems", pp. 532–535, 2002.

[9] H. Urey, "Torsional MEMS scanner design for high-resolution scanning display systems". In "Optical Scanning", volume 4773, pp. 27–37, SPIE, 2002.
URL `http://link.aip.org/link/?PSI/4773/27/1`

Chapter 4

Fabrication

4.1 Tilting Platform Device

4.1.1 Design Considerations

The tilting platform device is fabricated on SOI substrate by successive deep reactive ion etching (DRIE) of the device and of the handle layer, followed by a release etch of the buried silicon dioxide. In DRIE, large feature size variations affect the aspect ratio dependent etch rate. Best etching uniformity is achieved by etching narrow trenches with constant width throughout the design. We therefore structure the different parts of the device like the combs, the platform, and the torsion bars by etching trenches around the desired structures. Besides these structures, dummy silicon pieces are created which will be removed later in the fabrication process by underetching of the buried silicon dioxide.

The trenches that are etched in the device and in the handle layer have to be placed in such a way that the stability of the device is not affected. For a good stability, the trenches in the device and in the handle layer have typically a lateral offset of at least 300 µm. The size of the top static comb electrodes has to be chosen large enough

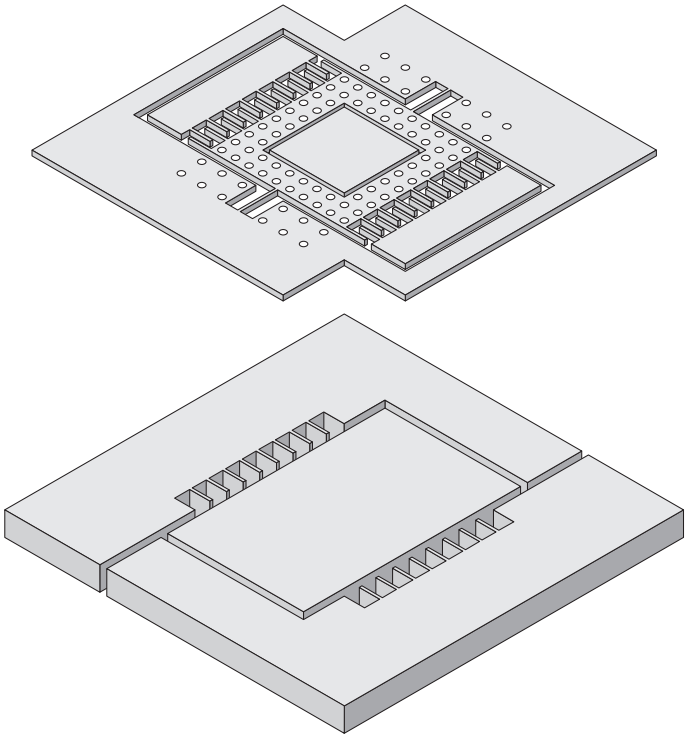

Figure 4.1: *Exploded view of the device and the trenches etched in the device (top) and in the handle layer (bottom). The device layer contains the platform with the torsion bars and the combs, and two static electrodes which are electrically isolated by surrounding trenches from the substrate. The handle layer contains the two backside static electrodes and a huge block to protect the platform during fabrication.*

to prevent them from being released when underetching the buried silicon dioxide.

The fabrication of the tilting platform device turned out to be critical due to the large size of the platform and the resulting leverage effect onto the torsion bars. The exposure to fluidic flow during the release etch of the buried silicon dioxide in BHF caused the torsion bars to break. A solution to this problem was found by using hydrofluoric (HF) vapor etching to remove the buried silicon dioxide. The process is presented in detail in Sec. 4.1.2. Another problem encountered during fabrication was related to dicing of the wafer into individual dies. The heavy vibrations that occurred during dicing destroyed the fragile torsion beams. The problem could be solved by introducing a new chip release process where dicing is not required anymore. The chip release process is presented in detail in Sec. 4.1.3. The stability of the device during fabrication could further be improved using a support structure in form of a huge silicon block underneath the platform. The silicon block is attached via the buried silicon dioxide to the platform and to the bulk area next to the platform such that the platform is temporarily fixed during the fabrication process. At the end of the fabrication process, the support structure is removed in the release etch of the buried silicon dioxide.

4.1.2 Hydrofluoric Vapor Phase Etching

The use of HF vapor phase etching enables the removal of silicon dioxide in a vaporous environment rather than in an aqueous solution [1–5]. This is of particular interest since one of the main problems referred to as stiction can be avoided. Stiction is often an irreversible and destructive phenomenon that occurs whenever liquids evaporate and pull down mobile structures to the substrate by means of surface tension. When silicon dioxide is etched in aqueous HF, rinsing in deionized water must follow to remove contaminants. Unfortunately water is characterized by a very high surface tension. Several methods have been reported that aim to reduce surface tension or

to avoid the transition from liquid to gaseous state of aggregation by employing either super critical drying or freeze drying.

First experiments on vapor phase etching were carried out by Holmes & Snell [1] in 1966. They observed that silicon dioxide on a wafer is etched with a comparable etch rate even when the wafer is not in the etch bath but close to. Helms & Deal [2] established that the role of water is to provide a condensed solvent medium for the HF on the surface. Offenberg *et al.* [3] proposed a two step reaction where first the silicon dioxide surface is opened by formation of silanol groups by adsorbed H_2O. Subsequently silanol groups are attacked by the HF:

$$SiO_2 + 2H_2O \rightarrow Si(OH)_4$$
$$Si(OH)_4 + 4HF \rightarrow SiF_4 + 4H_2O$$

The formula shows that water is at the same time initiator and reactant of the etching process. This fact suggests that the etching process can be temperature controlled in order to maintain the equilibrium of H_2O needed to initiate the process and H_2O produced in the reaction. The etch rate of silicon dioxide in HF vaporous environment depends strongly on the wafer temperature. Below 35°C we observed condensation, above 45°C no etching took place at all. Within this temperature range the etch rate can be accurately controlled by temperature.

The set-up consists of a Teflon chuck onto which a Kapton heating foil and a temperature sensor are glued. A heat sink in form of a 4-inch plate of stainless steel on top of the heating foil enhances the temperature homogeneity and seals the heating system. The wafer to be etched is loaded onto a dummy wafer on top of the stainless steel plate and fixed with a Teflon ring that is screwed onto the chuck. Then the whole set-up is put upside down onto a beaker containing 50% of HF dissolved in water. A feedback system enables to maintain a stable temperature during the entire process.

4.1.3 Dicing Free Chip Release Process

MEMS devices contain often very fragile mobile parts resulting in a high sensitivity to shock, vibration, and fluidic flow. One of the major problems encountered in the past is related to dicing of the wafers in order to separate the chips from each other. Since dicing is carried out at the end of the fabrication process, all mobile structures are already released. One way of protection consists in embedding the chips in resist prior to dicing. This method protects well the fragile structures during dicing but stripping of the resist afterwards in acetone and isopropyl alcohol is very critical. Dicing debris deposited onto the resist during dicing have the tendency to settle down on the silicon surface when the resist is stripped in acetone. This must be avoided since these particles can potentially create short circuits or block mobile parts. In addition, stripping of the resist followed by rinsing is risky due to stiction of the mobile parts to the substrate.

A novel method of a clean chip release process was therefore developed where dicing is not needed anymore. The chip release process requires that both the device and the handle layer of a SOI wafer are structured by DRIE. The additional trenches and holes required for the chip release process can be etched simultaneously with the device structures, i.e. no additional process steps are needed. The contours of the chips are defined by trenches that are etched into the device and into the handle layer. The trenches in the device and in the handle layer are laterally offset by about 30 µm for stability reasons. Adjacent chips are arranged such that a silicon grid of several hundred micrometers width is formed between the chips. For each chip, the silicon grid contains two enlarged corner areas in the device layer that are perforated with a hole pattern. During fabrication, the chips are connected through the buried silicon dioxide to the enlarged corner areas of the silicon grid. In order to separate the chips from the wafer, the wafer is exposed to vaporous HF which penetrates through the holes and underetches the buried silicon dioxide.

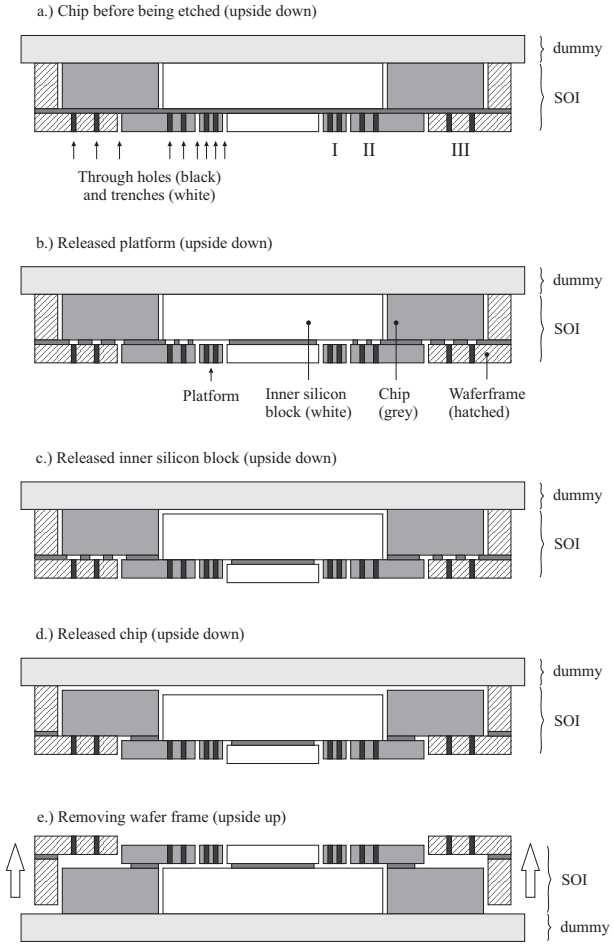

Figure 4.2: *3-stage HF vapor phase release process. Due to the different spacing of the holes, the silicon dioxide is successively removed in zone I, then in zone II, and finally in zone III. The detached parts can not come off since their handle layer is always larger. Finally, the chuck with the clamped wafer is turned up and the remaining wafer frame is unloaded. Then, the chips can be unpicked, and the backside block remains on the chuck.*

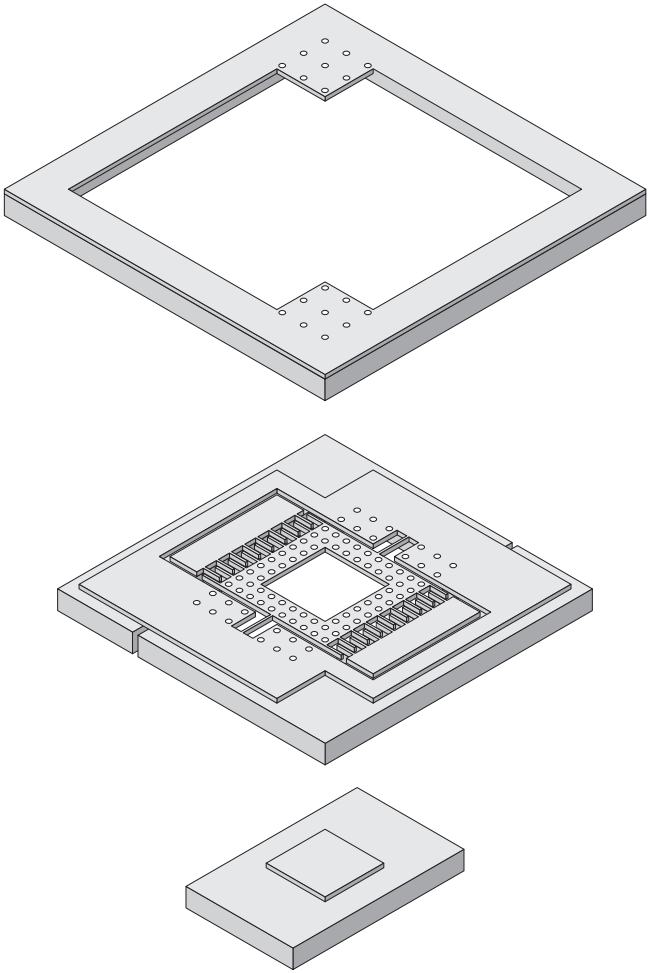

Figure 4.3: *The three different parts which are released one after another. First the platform is released from the backside block, then the backside block is detached from the frame, and at last the chip is released from the wafer grid.*

In the case of the tilting platform device we extended the described chip release process to a three-step release process where first the platform is released from the support structure, then the support structure is released from the chip, and finally the chip is separated from the wafer. This extended process requires holes in the platform, in the bulk area next to the platform, and in the enlarged corner area of the grid, as depicted in Fig. 4.3. In order to achieve a homogeneous etch rate during DRIE, the holes have a constant size, but their density varies according to the three release zones. The hole density is the highest in the platform, medium in

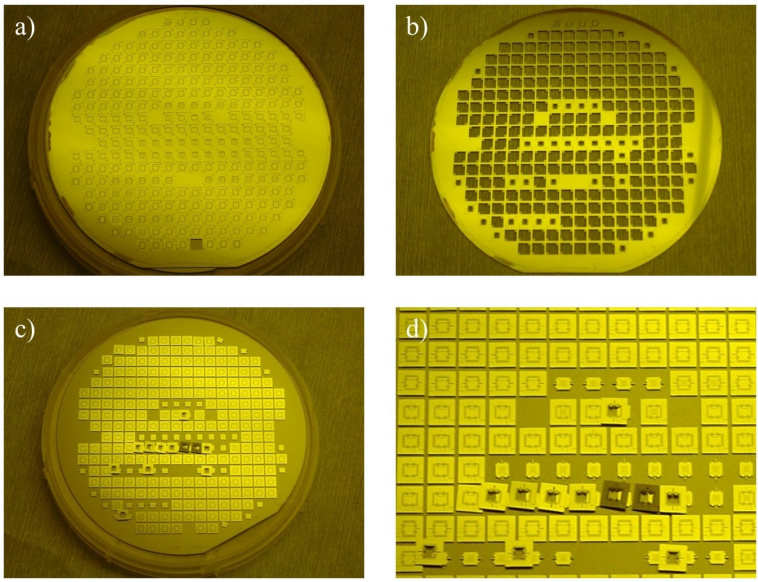

Figure 4.4: *a) Wafer with released chips after HF vapor etching; b) The detached wafer grid; c) The released chips; d) Detail of the released chips and the detached central bloc.*

the area next to the platform, and the lowest in the enlarged corner area of the grid. The different hole densities result in different underetching distances which are related to different etch times. Hence we can ensure that first the platform is detached from the support structure in the handle layer before the latter one is detached from the chip. This is important since we can make sure that the support structure with a mass several times higher than the one of the platform never exerts its weight onto the platform and the fragile torsion bars. Continued etching removes finally the buried silicon dioxide underneath the enlarged corner area of the grid such that the chips are completely detached from the wafer.

4.1.4 Microfabrication

The fabrication of the tilting platform device starts with a SOI wafer which has a device layer thickness of 75 µm, a buried silicon dioxide thickness of 2 µm, and a handle layer thickness of 350 µm. The thickness of the device layer results from the target tilt angle of ±4°and calculates according to Eq. 3.1. The handle layer thickness of 350 µm is a good compromise between wafer stability and a thickness which can still be etched with satisfying results in terms of verticality of the sidewalls. In order to improve the verticality of the 350 µm high backside combs, we first structure the handle layer, and second the device layer.

The structuring of the 350 µm thick handle layer requires a combined mask of photoresist and silicon dioxide. We therefore start the fabrication process with a thermal oxidation of 1 µm. Then we spin coat a 6.8 µm thick layer of AZ 4562 photoresist (AZ Electronical Materials) onto the handle layer. The photoresist is patterned by photolithography and developed in a basic developer solution. The photoresist patterns thus created are then transferred into the silicon dioxide by etching the uncovered regions in buffered hydrofluoric acid (BHF). For BHF etching we use a special chuck which protects the silicon dioxide on the device layer from being etched. This is done because the silicon dioxide to be removed on the handle layer

represents less than 5% of the wafer surface. Hence, wafer bowing induced by stress due to an unbalanced amount of silicon dioxide on the device and on the handle layer can be reduced. The wafer bow has to be kept as small as possible in order to ensure a good alignment for the following photolithography. Besides, a lot of automated clean room equipment works with vacuum handlers which encounter a lot of problems with bowed substrates.

Once the double mask of photoresist and silicon dioxide is patterned, the handle layer is structured by DRIE, followed by an oxygen plasma cleaning to remove photoresist residues. Then, a 6.8 µm thick layer of AZ 4562 photoresist is spin-coated onto the device layer. The following photolithography requires an accurate backside alignment of the mask onto the structures already etched in the han-

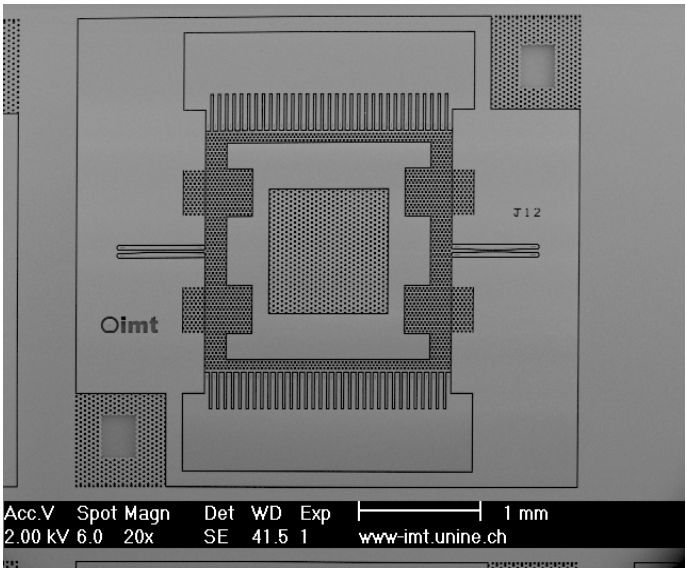

Figure 4.5: *SEM picture of the device layer after DRIE.*

dle layer. The alignment is critical since the mobile combs in the device layer have to be aligned with the static combs in the handle layer. In the best case we achieved an alignment accuracy better than ± 1 µm. After development of the exposed photoresist, the patterns are again transferred into the silicon dioxide by BHF etching using a chuck to protect the handle layer from being etched. The device layer is then structured by DRIE, followed by oxygen plasma cleaning to remove photoresist residues.

During DRIE, silicon spikes are sometimes formed in the etched trenches which can cause short circuit in the case they happen to be in the comb structure. For this reason the structured wafer is thermally oxidized, and the silicon spikes are thus transformed into silicon dioxide. Finally, a release etch of the buried silicon dioxide

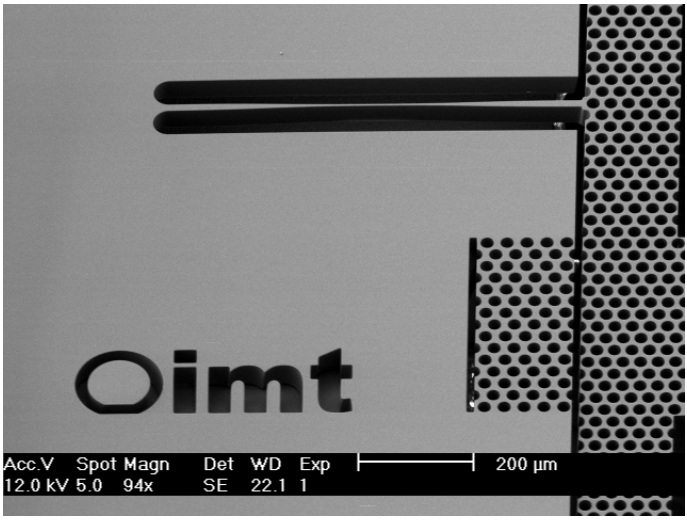

Figure 4.6: *SEM picture showing in detail the hourglass-shape of the torsion beam. The particular shape of the torsion beam increases considerably the lateral stability of the platform.*

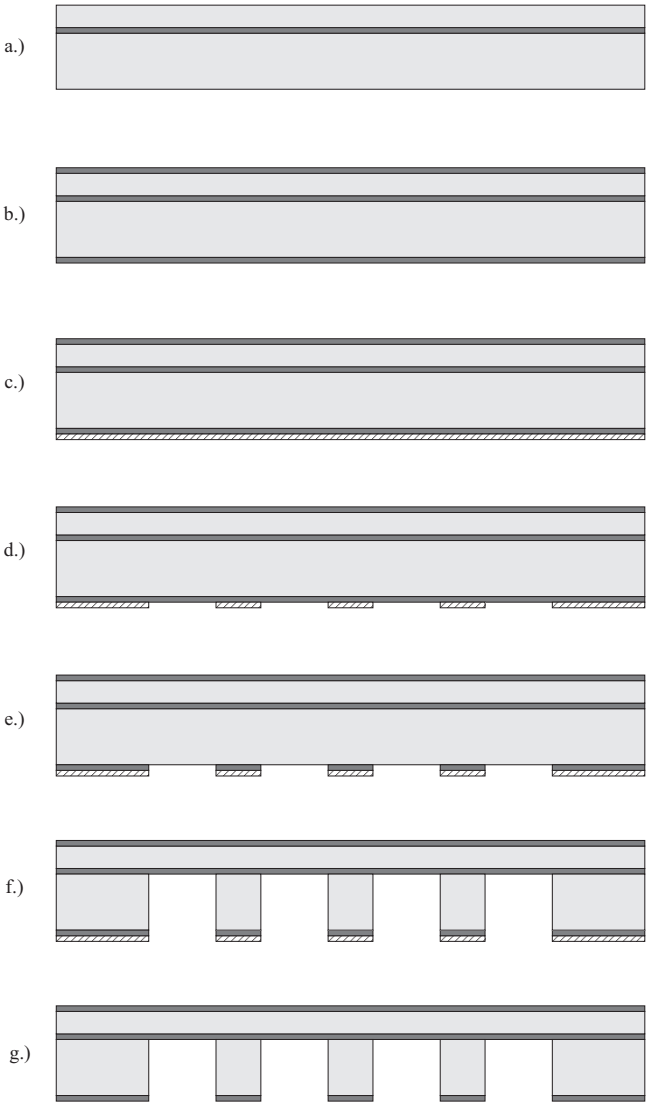
a.)
b.)
c.)
d.)
e.)
f.)
g.)

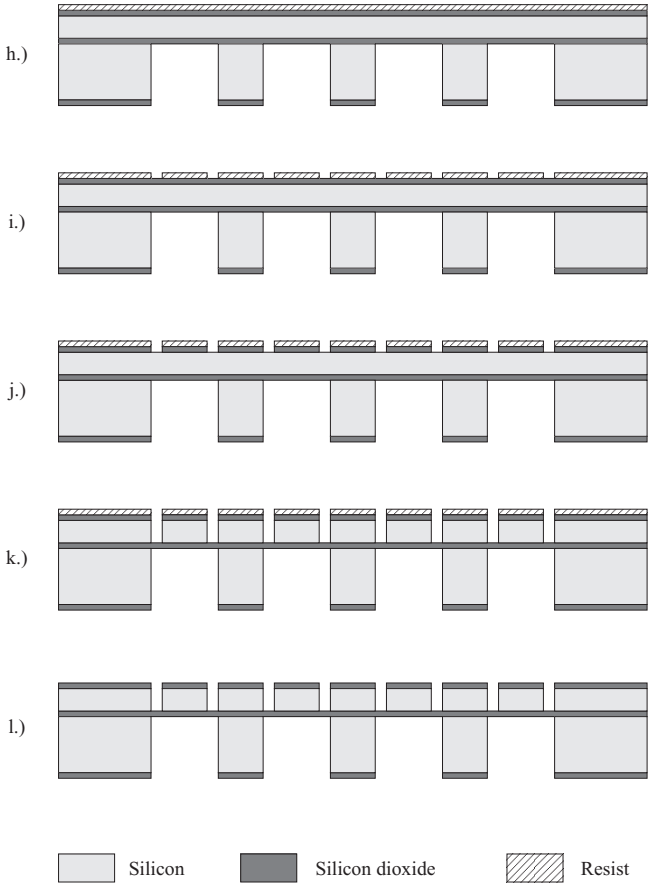

Figure 4.7: *Process sequence for the fabrication of the tilting platform device: a.) blank SOI wafer, b.) thermal oxidation, c.) spin-coating of photoresist onto handle layer, d.) photolithography, e.) BHF etching of silicon dioxide, f.) DRIE, g.) photoresist removal, h.) spin-coating of photoresist onto device layer, i.) photolithography, aligned on backside structures, j.) BHF etching of silicon dioxide, k.) DRIE of device layer, l.) photoresist removal.*

using HF vapor etching is performed. Hence the platform is released, and the dies are separated from the wafer.

4.1.5 Assembly

For assembly and testing of the devices we fabricated PCBs with the same footprint like the MMC *Multimedia Memory Cards* used for data storage in portable devices. This allows us to use inexpensive accessories like card connectors or antistatic storing boxes. The MMC card connectors are reliable and offer a good prealignment. Using this system, no connectors or other parts have to be soldered onto the PCBs. This is quite important since the assembly set-up used to glue the filter on the MEMS device requires that nothing exceeds the height of the MEMS device. Soldering after assembly

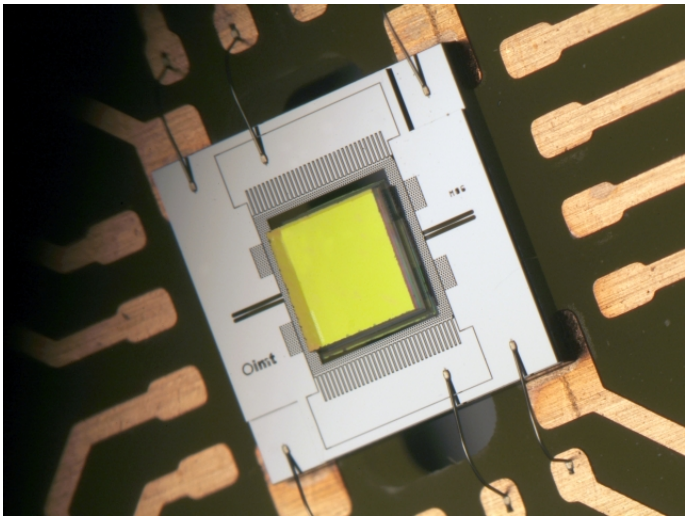

Figure 4.8: *Photograph of the MEMS chip which is glued and wire-bonded onto a PCB and assembled with the RGF.*

of the filter is not convenient either, since solder-forming flux could potentially deposit onto the filters, making them unusable.

The MEMS device is first glued onto the PCB using a two component epoxy glue. Then, the MEMS device is wirebonded onto the copper pads of the PCB. A hole in the PCB underneath the platform is provided for optical transmission.

The set-up for assembling the filter onto the MEMS device is installed under a microscope. It is composed of a transparent vacuum pick-up tool and a fine wire, both mounted on individual xyz-tables. First, the wire is immersed in a droplet of UV curable glue. Then the glue attached to the wire is deposited at the corners of the platform. Afterwards, a filter is picked up with the vacuum tool and positioned on the glue droplets. The vacuum is then released and the pick-up tool lifted up. Finally, the glue is cured with a UV lamp through the filter.

4.2 Piston Tip-Tilt Mirror Device

4.2.1 Design Considerations

In the piston tip-tilt mirror device, all device relevant structures are fabricated in the device layer of an SOI wafer. Parts of the silicon structures like the mobile combs and the curved beams have to be thinned down during the fabrication process. For this purpose we developed a process that allows to etch a step profile of a defined height into the silicon. This step is then transferred into the bulk with the relative height differences being preserved. The process is presented in detail in Sec. 4.2.2 and features self-alignment of the two masks used to etch the step profile. The self-alignment feature yields a very good alignment accuracy of the comb actuators, in contrast to the comb actuators in the tilting platform device which are backside aligned.

The required structures that have to be etched into the handle layer are much less critical than those needed for the tilting platform device. Besides large channels that separate the dies from the bulk silicon according to the chip release process discussed in Sec. 4.1.3, a huge hole is etched into the handle layer underneath the mirror. The hole has the same footprint than the mirror and serves to reduce the area where the mirror is attached via the buried SiO_2 to the handle layer. In order to release the mirror, the buried SiO_2 underneath the mobile combs (see Fig. 3.13) has to be removed in HF vapors.

Another feature concerns the rounded shape of the etched silicon structures which enhances strongly the etching homogeneity due to a very uniform gas exchange during DRIE.

4.2.2 Self-Aligned Delay Mask Process

The delay mask process is a technique where a stack of two masks is applied on top of each other prior to DRIE. The DRIE process is stopped once the desired step in the silicon is reached, and the top mask is removed before continuing DRIE with only the remaining

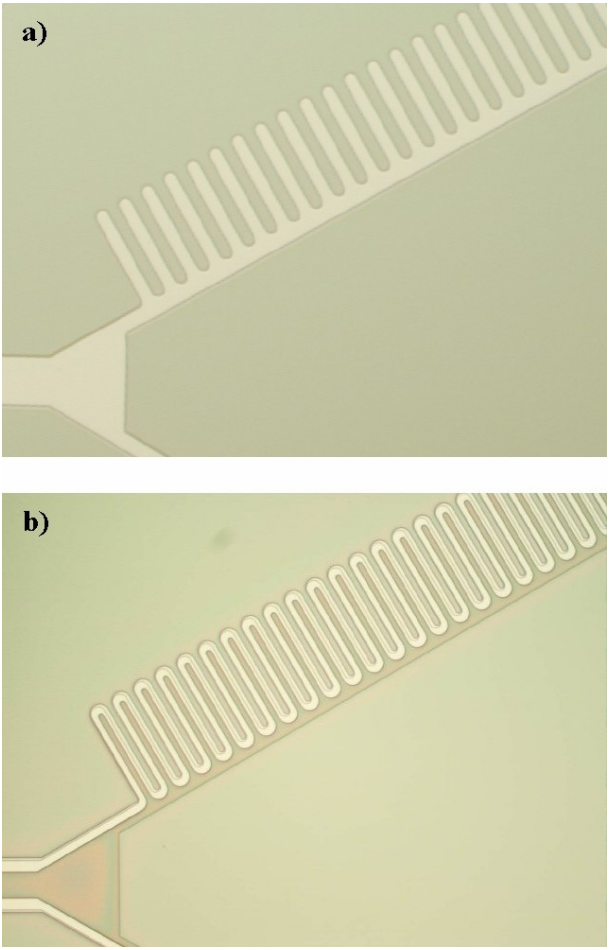

Figure 4.9: *The two masks used for the delay mask process: a) the SiO_2 is removed where the mobile combs will be located (bright area); b) another resist mask is applied on top of the SiO_2, containing the same structures like mask a), but additionally also the mobile combs (brownish area). The SiO_2 is re-patterned with mask b).*

mask. Hence the step profile created at the surface is transferred into the bulk with the relative height difference being preserved. The term delay mask refers to the patterns which start being etched with a delay once the top mask is removed.

Kwon *et al.* [6, 7] reported on a delay mask process where the second mask is self-aligned to the first mask. This process is particularly interesting for the fabrication of our asymmetric vertical comb actuators since the mobile and the static combs can be perfectly aligned to each other. Kwon *et al.* used two types of patterned silicon dioxide films on top of each other where the thickness of the top silicon dioxide mask was calculated such that it was removed once the desired step profile was achieved. We modified the process with respect to the used materials and applied first a silicon dioxide mask, and second a photoresist mask.

The process for the self-aligned delay mask process starts with a thermal oxidation of the silicon substrate. Then, the silicon dioxide is locally removed at the positions where the silicon structures with the reduced height will be located. The patterns etched into the silicon dioxide are actually larger than the future silicon structures with the reduced height. According to Sec. 3.2.3, the minimum gap size between static and mobile combs is 5 µm, which allows to optimally oversize the opening in the silicon dioxide by 2.5 µm. Once the silicon dioxide is locally opened, the photoresist is removed, and a new photoresist layer is spin-coated for the second mask. This second mask defines entirely the lateral dimensions of the device. The oversized opening in the silicon dioxide ensures that the photoresist pattern defining the silicon structures with the step profile can be aligned towards the silicon dioxide pattern with a tolerance of ±2.5 µm in both x and y direction. Finally, the excess silicon dioxide is removed by anisotropic dry etching.

4.2.3 Microfabrication

The fabrication of the piston tip-tilt device starts with a SOI wafer which has a device layer thickness of 50 µm, a buried silicon dioxide thickness of 2 µm, and a handle layer thickness of 350 µm. Compared to the piston tip-tilt device, we reduced the device layer thickness from 75 µm to 50 µm since we had no design constraints for the mirror thickness. The reduction of the device layer thickness results in a reduced mass of the mirror and in an improved etch homogeneity of the sidewalls. In order to provide a double mask for the delay mask process, we start the fabrication sequence with a thermal oxidation of 0.6 µm, followed by spin coating a 1.8 µm thick layer of AZ1518 photoresist onto the device layer. In the subsequent photolithography we expose those areas where the silicon dioxide will be removed, i.e. where the mobile combs and the three suspension beams will be located. The silicon dioxide is removed by anisotropic dry etching. Then, the photoresist layer is removed in oxygen plasma prior to spin coating a new 1.8 µm thick layer of AZ1518 photoresist onto the device layer. Although this second layer is applied on a structured surface with 0.6 µm high silicon dioxide patterns, the uniformity is very good. The mask used to pattern the second photoresist layer contains the entire geometry of the device such that the mobile and the static combs are self-aligned. To finish the two level stack of masks, the remaining excess silicon dioxide borders are removed by anisotropic dry etching. Once the two masks are prepared, a step of approximately 15 µm is etched into the device layer by DRIE. Then the DRIE process is stopped and the photoresist mask is stripped in oxygen plasma. Subsequently the DRIE process is continued with the remaining silicon dioxide mask until the buried silicon dioxide is reached. Hence the step profile created at the surface is transferred into the bulk silicon.

The structuring of the 350 µm thick handle layer by DRIE requires a combined mask of photoresist and silicon dioxide. Since the silicon dioxide is still present on the handle layer, we continue the fabrication process by spin coating a 6.8 µm thick layer of AZ4562

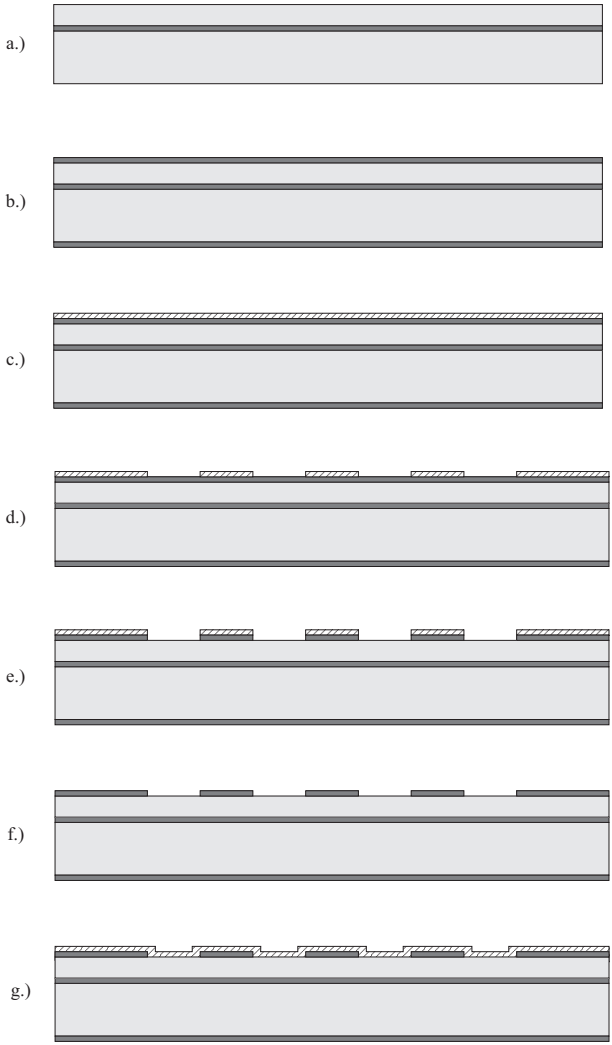
a.)
b.)
c.)
d.)
e.)
f.)
g.)

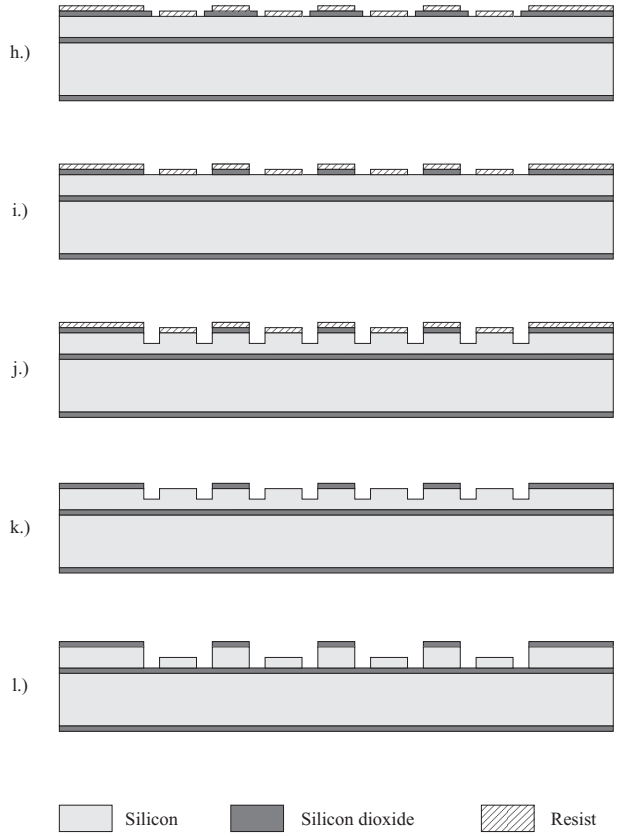

Figure 4.10: *Process sequence for the fabrication of the piston tip-tilt mirror device: a.) blank SOI wafer, b.) thermal oxidation, c.) spin coating photoresist onto device layer, d.) photolithography, e.) anisotropic dry etching of SiO_2, f.) stripping photoresist, g.) spin coating photoresist onto device layer, h.) photolithography, aligned on SiO_2 patterns, i.) anisotropic dry etching of SiO_2, j.) timed DRIE, k.) stripping photoresist mask, l.) continuing DRIE with SiO_2 mask.*

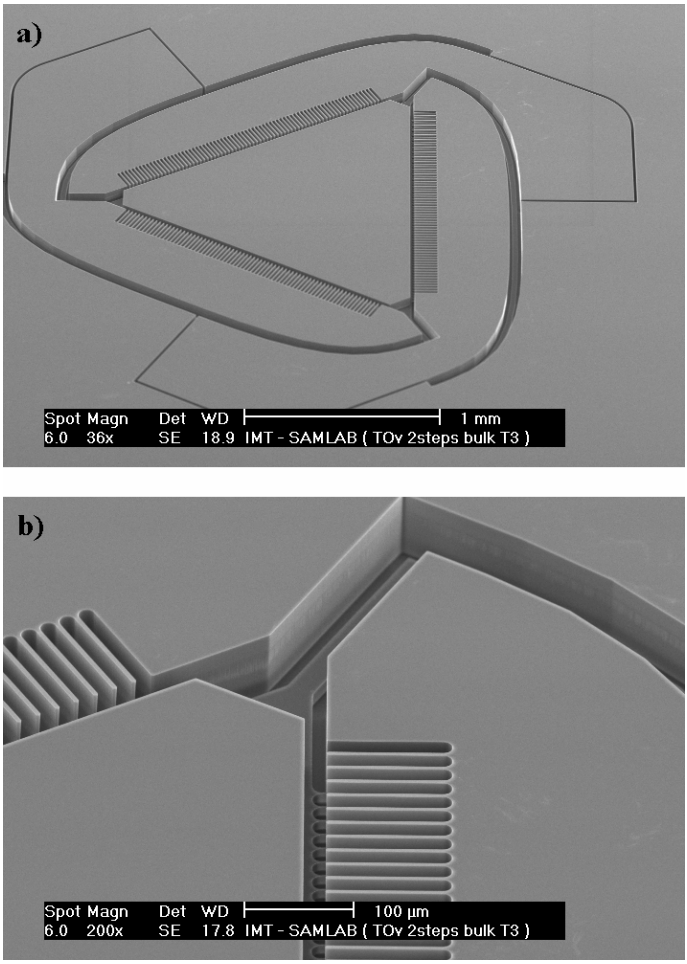

Figure 4.11: *a) SEM picture of device layer showing the triangular shaped mirror, the three C-shaped suspension beams, and the three static comb electrodes; b) Detail of etched down suspension beam and mobile combs.*

photoresist (AZ Electronical Materials) onto the handle layer. The photoresist is patterned by photolithography and developed in a basic developer solution. The photoresist patterns are then transferred into the silicon dioxide by anisotropic dry etching. The combined soft mask (photoresist) and hard mask (silicon dioxide) is sufficiently thick for the following DRIE process where channels are etched onto the buried silicon dioxide throughout the 350 µm thick handle layer.

In the following HF vapor etching step, the HF vapors penetrate through the channels etched into the silicon and underetch the buried silicon dioxide such that the mobile combs and the mirror are released from the handle layer. In the same step, the devices are separated from each other by using the chip release process discussed in Sec. 4.1.3.

Bibliography

[1] P. J. Holmes and J. E. Snell, "A Vapour Etching Technique for the Photolithography of Silicon Dioxide". *Microelectronics and Reliability*, **5**:337–341, 1966.

[2] C. R. Helms and B. E. Deal, "Mechanism of the HF/H2O vapor phase etching of SiO2". *J. Vac. Sci. Technol.*, **A10**(4):807–811, Jul/Aug 1992.

[3] M. Offenberg, B. Elsner, and F. Lärmer, "Vapor HF Etching for Sacrificial Oxide Removal in Surface Micromachining". In "Proc. Electrochemical Soc. Fall Meeting", volume 94-2, pp. 1056–1057, 1994.

[4] J. Anguita and F. Briones, "HF/H2O vapor etching of SiO2 sacrificial layer for large-area surface-micromachined membranes". *Sensors and Actuators*, **A64**(3):247–251, January 1998.

[5] A. J. Muscat, A. G. Thorsness, and G. Montaño-Miranda, "Characterization of residues formed by anhydrous hydrogen fluoride

etching of doped oxides". *J. Vac. Sci. Technol.*, **A19**(4):1854–1861, Jul/Aug 2001.

[6] S. Kwon, V. Milanovic, and L. P. Lee, "Vertical Microlens Scanner for 3D Imaging". In "Technical Digest of the Solid-State Sensor and Actuator Workshop", pp. 227–230, 2002.

[7] S. Kwon, V. Milanovic, and L. P. Lee, "Large-Displacement Vertical Microlens Scanner with Low Driving Voltage". *IEEE Photonics Technology Letters*, **14**(11):1572–1574, November 2002.

Chapter 5

Characterization

5.1 Tilting Platform Device

In this section we describe the characterization of the tilting platform device. First the tilt angle is evaluated in function of the applied actuation voltage. Then we characterize a device where a RGF is assembled on top of the tilting platform. We establish the relation between actuation voltage and the corresponding wavelength of the RGF's resonance peak and demonstrate tuning of the C-band. Finally, the accuracy of the measurements is discussed.

5.1.1 Characterization of MEMS Device

In order to evaluate precisely the tilt angle in function of the applied actuation voltage, we measure the vertical deflection z at the extremity of the platform and calculate the corresponding tilt angle which is then given by

$$\theta = \tan^{-1}\left(\frac{z}{R}\right) \tag{5.1}$$

Due to the large size of the platform ($R = 1000\,\mu m$), this indirect measurement of the tilt angle is quite precise. A vertical resolution of 1 µm corresponds to an angular resolution of 1 mrad (0.057 °).

Measurement Set-up

The vertical deflection of the platform was measured with an UBM optical profilometer. The optical profilometer performs a point measurement using a laser with a wavelength of $\lambda = 633\,nm$ which is focused onto the sample to be investigated. The backreflected laser beam passes through a lens which can be electromagnetically positioned. A pinhole is located behind the lens and in front of a second (fixed) lens and a detector. The optical system is designed such that the maximum intensity on the detector is only achieved when the focal point lies exactly in the plane of the pinhole. This is true for a well defined distance between the lens and the sample. As soon as this distance changes, the system repositions the lens, trying to maximize again the intensity on the detector. The current in the coil of the electromagnetically actuated lens correlates therefore with the distance between the lens and the sample. At its output, the profilometer provides a bipolar voltage of $\pm 10\,V$ corresponding to the absolute distance within a range of $\pm 50\,\mu m$. A second output provides a differential signal which can be used in combination with a lock-in amplifier to evaluate the resonance frequency. The differential signal allows only a qualitative evaluation of the resonance frequency rather than an amplitude measurement. The maximum frequency that can be detected is limited to 10 kHz.

Static Measurements

The angle-voltage characteristic was measured on two devices having different designs of the comb actuators according to Tab. 3.1. The device with 20 µm wide static combs was not functional, whereas the device with 30 µm wide static combs worked well. Investigations by SEM showed that the backside static combs suffered from notching,

as can be seen Fig. 5.1. The notching occurred only in the front part of the combs and was caused by overetching. The overetching was necessary in the rear part of the combs in order to etch the gap between the combs down to the box. The height reduction caused by notching was measured to be in the order of 15 µm in the design with 30 µm wide static combs, and more than 30 µm in the design with 20 µm wide static combs.

The angle-voltage characteristic of the device with 30 µm wide static combs is depicted in Fig. 5.2. The measurements were realized by applying a voltage, respectively, to the static backside comb number ③ for negative tilt angles, and to the static backside comb number ④ for positive tilt angles (see Fig. 3.2). All other comb electrodes were grounded. In both measurements a voltage ramp was applied to the corresponding backside comb, and the vertical displacement

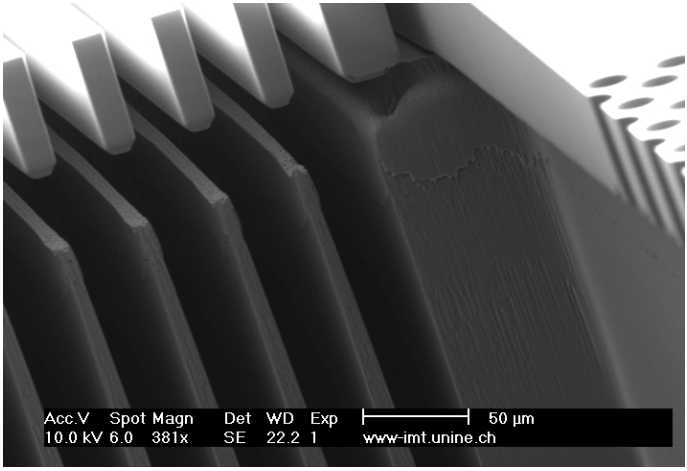

Figure 5.1: *Severe notching of the static backside combs for the device having 20 µm wide static combs. As a result, the available force is considerably reduced.*

was measured after each voltage increment. The power supply used to drive the comb actuators was a Keithley 2400 Sourcemeter which is characterized by a very low noise (10 Hz - 1 MHz) of 10 mV_{p-p}. We achieved a mechanical tilt angle of $\pm 3.5°$ at an actuation voltage of ± 80 V. At higher voltages the device became unstable resulting in in-plane rotation of the platform. The measured angle-voltage characteristic (blue graph) is in good agreement with the analytical approximation (red graph) established in Sec. 3.1.5. The deviation of the two graphs can be attributed to notching of the backside static combs in DRIE. Consequently, the available force for tilt angles smaller than 1 ° was considerably reduced.

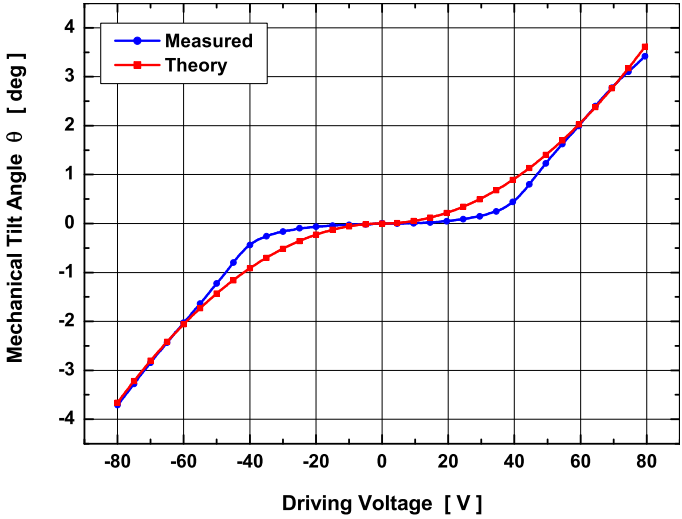

Figure 5.2: *Mechanical tilt angle θ versus applied actuation voltage. A voltage sweep was applied on comb ③ for negative tilt angles, and on comb ④ for positive tilt angles. The deviation from the analytically approximated graph is due to notching of the combs.*

Dynamic Measurements

The resonance frequency was evaluated using the optical profilometer in combination with a lock-in amplifier (Stanford Research System SR850), and the result is depicted in Fig. 5.3. The differential output signal of the profilometer was connected to the input of the lock-in amplifier. The output of the lock-in amplifier was used to drive the mobile combs ⑤ attached to the tilting platform. The driving signal V_d provided by the lock-in amplifier was a bipolar sine signal with an amplitude of $10\,V_{p\text{-}p}$ that was swept from 1 Hz to 410 Hz. The two static backside comb electrodes ③ and ④ were biased with +5 V and - 5 V, respectively. With the chosen combination of sine amplitude and bias voltage we could achieve that during half a period the platform is pulled down to one side, and during the other half period the platform is pulled down to the other side. With this set-up we measured a resonance frequency of 208 Hz.

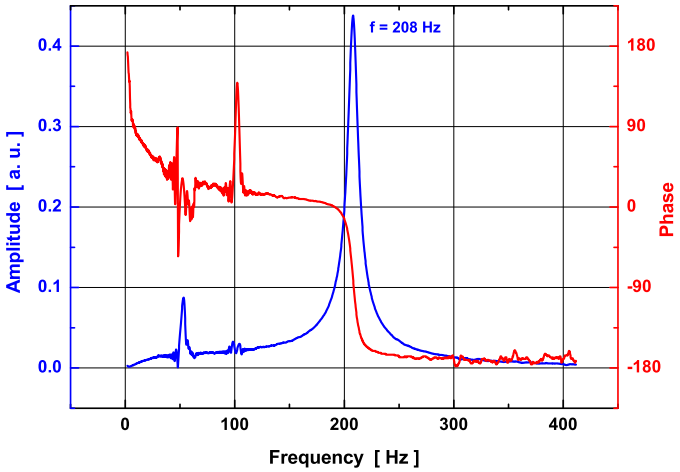

Figure 5.3: *Resonance frequency and corresponding phase diagram of the tilting platform device.*

5.1.2 Characterization of Filter Device

The following section describes the optical set-up and the measurements that were carried out on a tilting platform device which was assembled with an RGF. The aim of these measurements is to establish the relation between the actuation voltage used to tilt the RGF, and the wavelength of the RGF's resonance peak which shifts in function of the tilt angle.

Set-up

The measurement set-up used for the characterization of the MEMS tunable filter device is shown in Fig. 5.4. A tunable laser source

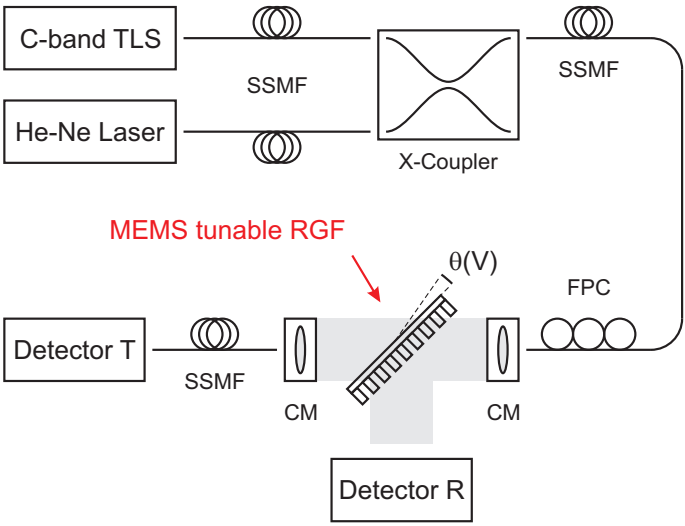

Figure 5.4: *Schematic of the measurement set-up and used abbreviations. TLS: Tunable Laser Source; SSMF: Standard Single Mode Fiber; FPC: Fiber Polarization Controller; CM: Collimator.*

(Nettest Tunics Purity) covering the C- and the L-band is connected by the intermediate of a 3 dB coupler to a fiber polarization controller using standard single mode fibers. The 3 dB coupler is used to couple the (visible) light of a He-Ne laser into the same fiber in order to facilitate the manual optical alignment of the MEMS tunable filter device in the optical path. The polarization controller is provided to optimize the intensity for TE polarization where the polarization dependent RGF has its maximum performance. The output of the polarization controller is connected with another single mode fiber to a custom-built stage providing an aligned input and output port,

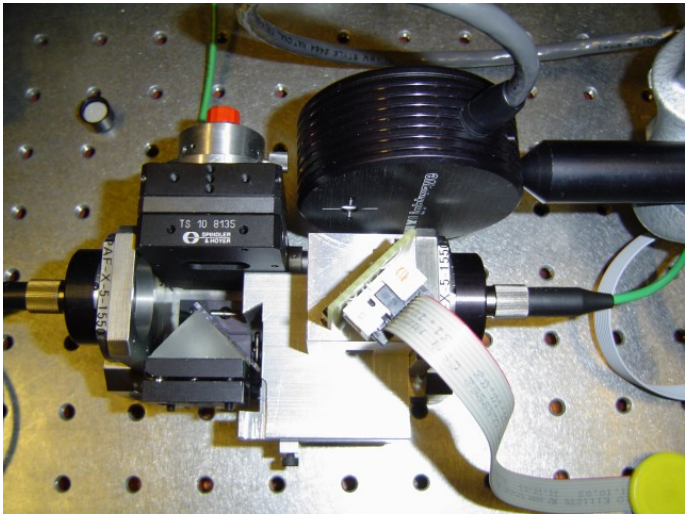

Figure 5.5: *Custom built optical bench providing aligned FC fiber input (left) and output (right) connectors equipped with collimators. The MEMS device with the RGF is mounted at 45° in the optical path. The big detector in the center of the picture records the reflected signal. The third fiber port (with red cap) as well as the prism are not used.*

both equipped with FC fiber connectors and collimators (Fig. 5.5). The first collimator is used to extend the beam size on the filter. The second collimator is used to recollect the light and to couple the light into the fiber output port.

The free space distance between input and output port measures 10 cm. The MEMS device with the RGF on top is mounted at 45 degrees in the optical path between input and output port. The output port used to record the transmitted power is connected with a fiber to an ILX Lightwave FPM-8200 power meter with integrated InGaAs sensor. The reflected power is recorded using an ILX Lightwave OMM-6810B power meter with OMH-6727B InGaAs power/wavehead. This power/wavehead is equipped with an integrating sphere that makes it suitable for accurate free-space power and wavelength measurements. Hence, the measured power of the reflected laser beam does not change in function of the angle of incidence. The MEMS tilting device is operated with a Keithley 2400 Sourcemeter. The sourcemeter provides a programmable digital I/O port which we use to drive a relay in order to switch the actuation voltage to either of the two backside static comb electrodes such that the platform can be tilted either to the right or to the left side.

The instruments used in this set-up are all equipped with a GPIB programming interface. This interface is quite useful in this set-up since we have to control five instruments and collect data from them in a timed measurement sequence. For this purpose we wrote a program in Visual Basic based on the SCPI language (Standard Commands for Programmable Instrumentation) which is well embedded in the GPIB IEEE-488.2 environment.

Measurements

In a first series of measurements we set the actuation voltage that was applied to one of the static backside combs ③ or ④ to a certain value and scanned the wavelength of the tunable laser from 1530 nm to 1570 nm (telecom C-band) in increments of 0.2 nm. After each wavelength increment, the actuation voltage, the wavelength, and

both the optical power in transmission and reflection were recorded. This measurement was repeated for different actuation voltages, and the measurement results are shown in Fig. 5.6. For better visibility, only the reflected peaks are shown, although the reflected and the transmitted values have been recorded. The different colored graphs in Fig. 5.6 correspond to different angular positions of the RGF that were achieved with the indicated actuation voltages. The relative small signal (peak height) and the oscillations are related to a non-optimized spot size of the laser on the filter due to manipulation

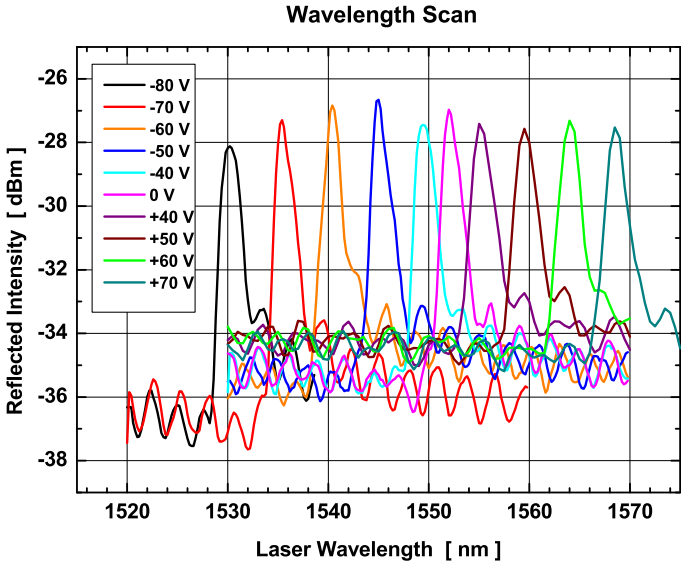

Figure 5.6: *Spectral reflectivity of the RGF. The different color coded graphs were obtained by scanning the wavelength of the tunable laser over a broad spectral range in increments of 0.2 nm, while the actuation voltage on the MEMS device was fixed to the indicated values.*

problems with the collimator.

In another series of measurements we fixed the wavelength of the tunable laser to different values and performed a voltage scan on the static backside combs ③ and ④. The corresponding measurement results are depicted in Fig. 5.7. The peak broadening of the reflected laser at low actuation voltages is due to the quadratic response of the tilting platform.

In order to estimate the tuning resolution achieved with the MEMS tilting platform, we calculated, respectively, the spectral width in Fig. 5.6 of the different reflection peaks at -3 dB attenuation, and the voltage span in Fig. 5.7 of the corresponding peaks,

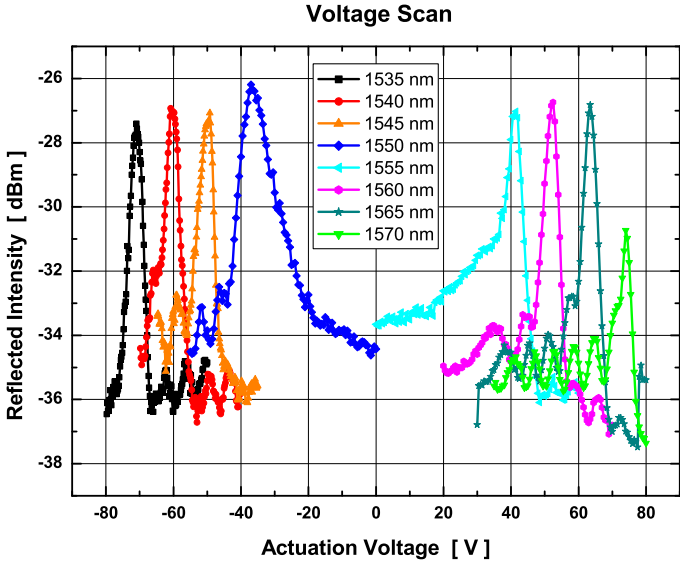

Figure 5.7: *Spectral reflectivity of the RGF. In these measurements, the wavelength of the laser was fixed, and the actuation voltage on the MEMS device was scanned within a selected voltage range.*

again at -3 dB attenuation. The ratio of spectral width and number of increments within the voltage span yields a tuning resolution of ≤ 0.1 nm. In terms of tilt angle, the tuning resolution was calculated to be $\leq 0.02\,^\circ$ using the RGF's tuning slope of 5.83 nm/°.

5.1.3 Accuracy of the Measurements

A graphical estimation of the measurement accuracy can be achieved by comparing the angle-dependent spectral reflectivity of the RGF for different measurement methods. In Fig. 5.8, the black graph was

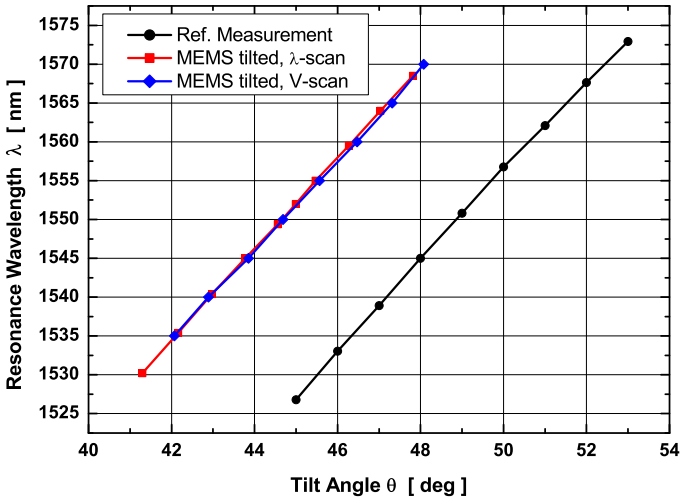

Figure 5.8: *Spectral reflectivity of the RGF, evaluated by tilting the RGF using a rotation stage (black graph), and by tilting the RGF with the MEMS device (red and blue graph). The measurement points of the red and blue graphs form a straight line having the same slope than the black graph. This shows that the measurements carried out on the MEMS device and on the assembled filter device are very accurate.*

obtained by tilting the RGF using a precise rotation stage. The red and the blue graph were obtained by tilting the RGF with the MEMS device.

The red graph is based on the measurements in Fig. 5.6 that are combined with the measurements in Fig. 5.2. First we read out the central wavelength of the reflection peaks in Fig. 5.6 which are related to the indicated actuation voltages. Then, we established the relation between the different actuation voltages and the corresponding tilt angles using Fig. 5.2. Hence we obtained the relation between the central wavelength of the reflection peaks, and the corresponding tilt angles.

The blue graph is based on the measurements in Fig. 5.7 that are combined with the measurements in Fig. 5.2. First we read out the voltage values of the peak maxima in Fig. 5.7 which are related to the indicated central wavelength. Then, we established the relation between the different actuation voltages and the corresponding tilt angles using Fig. 5.2. Hence we obtained the relation between the central wavelength of the reflection peaks, and the corresponding tilt angles.

The fact that the measurement points of the red and the blue graph form a straight line having the same slope than the black graph shows well that the individual measurements in Fig. 5.6, Fig. 5.7, and Fig. 5.2 are very accurate. The shift of the black graph with respect to the red and to the blue graph is related to an angular offset. The slope of the three graphs was measured to be $5.83\,\mathrm{nm}/^{\circ}$.

5.2 Piston Tip-Tilt Mirror Device

This section describes the characterization of the piston tip-tilt mirror device. For characterization we used two different contactless optical methods. First, we analyzed the vertical displacement of the mirror with an optical profilometer. The used instrument measures the vertical displacement at a single point using a focused He-Ne laser beam having a spot size of approximately $10 \times 10\,\mu m^2$. Although more powerful instruments providing 3D topographic measurements are available, this single-point measurement is interesting since the measurements are performed very quickly. Hence it is well suited to establish the relation between actuation voltage and vertical displacement with many measurements in a reasonable time. On the other hand, no information about the flatness of the mirror or the tip-tilt is provided. For this reason we performed for some actuation voltages an accurate 3D topographic measurement using a Wyko NT3300 optical profiler.

5.2.1 Point Measurement of Displacement

The vertical displacement of the mirror in the piston mode was analyzed with the point profilometer described in Sec. 5.1.1. A voltage sweep from 0 to 80 V in increments of 0.5 V was applied to all three static comb electrodes, and the vertical displacement was measured with the point profilometer after each voltage increment. The corresponding graph in Fig. 5.9 shows the resulting vertical displacement of the mirror. The graph refers to the device having 3×52 mobile combs with gaps of $g = 7\,\mu m$ and a grounded substrate underneath the combs. The measured vertical displacement (blue graph) shows a small deviation from the analytical approximated model (red graph). The deviation is related to an increased gap between the static and the mobile combs caused by an additional cycle of oxidation and oxide removal. In order to prevent the chips from being destroyed due to electrical short circuit, we did not apply a higher actuation voltage than 80 V.

Dynamic Measurements

The resonance frequency was evaluated with the same set-up as already discussed in Sec. 5.1.1. The actuation voltage generated by the lock-in amplifier was a bipolar sine signal with an amplitude of $2.5\,V_{rms}$ that was swept from 1 Hz to 640 Hz. With a sweep time of 40 seconds and the used sampling frequency of 16 Hz the recorded amplitude has a resolution of 1 measurement/Hz. In contrast to the dynamic measurements performed on the tilting platform device, the static comb electrodes were not biased. As a result, the device sees twice the frequency due to the bipolarity of the used sine signal. This has to be taken into account in the amplitude - frequency

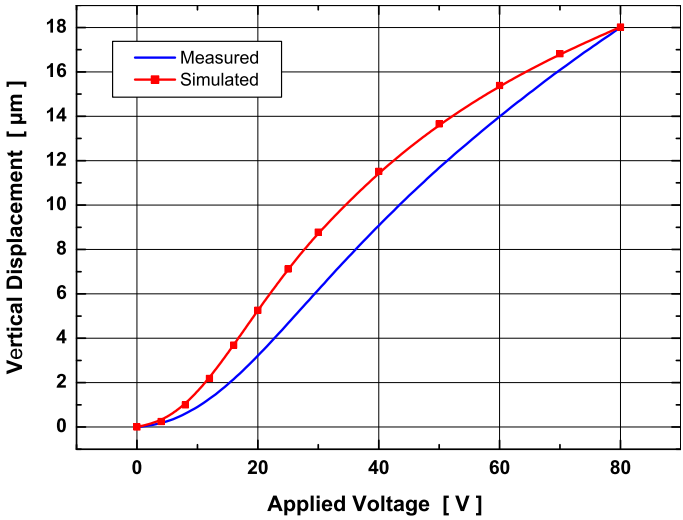

Figure 5.9: *Measured vertical displacement (blue graph) and simulated displacement (red graph). The results refer to the device with $N = 3 \times 52$ combs, gap $g = 7\,\mu m$, and a grounded substrate underneath the combs.*

plot of Fig. 5.10 by multiplying by a factor of 2 the frequency values associated to the corresponding amplitude values.

5.2.2 3D Topographic Measurements

The piston tip-tilt mirror device has been characterized with a Wyko NT3300 white light interferometer. This optical profiler provides 3D topography measurements with vertical resolution of 0.1 nm. Prior to the measurements, an eventual tilt between the sample and the instrument's optics has to be corrected in order to increase the vertical resolution. The tilt is visualized by interference fringes. The number of interference fringes is proportional to the degree of tilt, while the normal vectors to the interference fringes indicate the direction of tilt. Once the tilt is roughly reduced with the motorized stage, the remaining tilt is finally eliminated on a software level by selecting a zone on the sample which is then virtually flattened. In

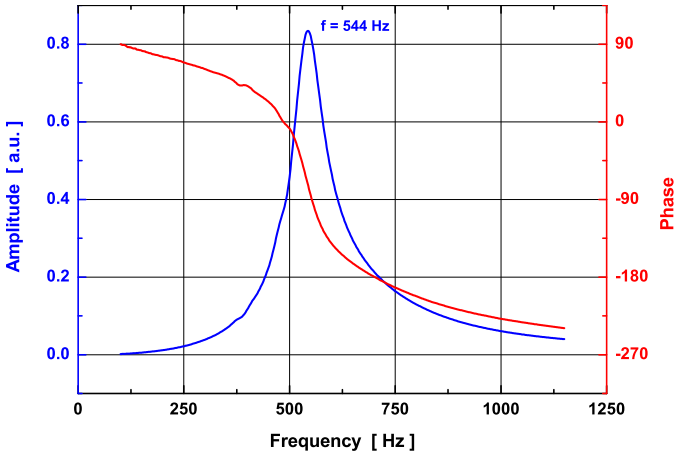

Figure 5.10: *Resonance frequency and corresponding phase diagram of the piston tip-tilt mirror device.*

our case it was difficult to define a flat zone since our device is bowed. This is also illustrated in Fig. 5.11 by the closed circular interference rings. The only part of the device which seems to be flat is the triangular mirror, where the interference fringes form parallel straight lines indicating a small tilt. Since we want to investigate the mirror, we can not use the mirror at the same time as a flat reference plane. For this reason we defined the reference plane by the red dots in Fig. 5.11 who are on the same height level since they are located on the same interference ring.

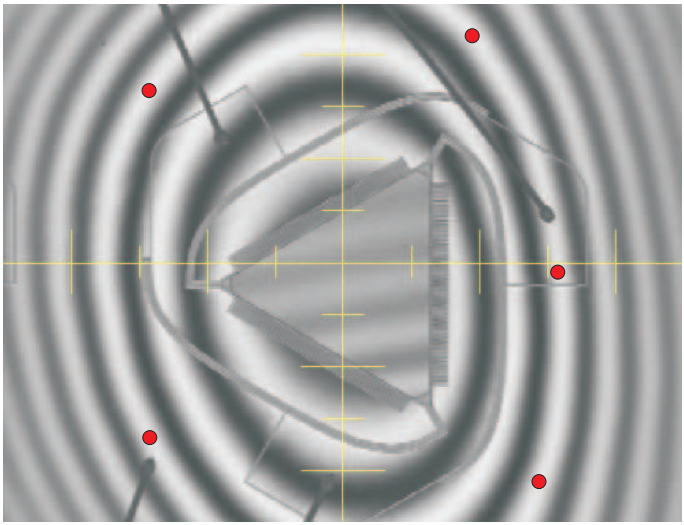

Figure 5.11: *Interference fringes on the piston tip-tilt mirror device. The circular interference rings indicate that the whole device is bowed, except the mirror where the interference fringes form parallel straight lines indicating a tilt between the sample and the instrument's optics. The planar reference plane is defined by the red dots.*

Piston Motion

In order to characterize the piston motion, we applied an actuation voltage to the three static comb electrodes. The mobile comb electrode (i.e. the mirror) was grounded. The 3D topographic profile of the device for different actuation voltages is depicted in Fig. 5.12. In picture a) one can see that the unactuated mirror (0 V) is slightly lower than the adjacent static comb electrodes. This is not due to gravity, but rather due to the fact that the height level of the mirror has to be measured with respect to the attachment points of the

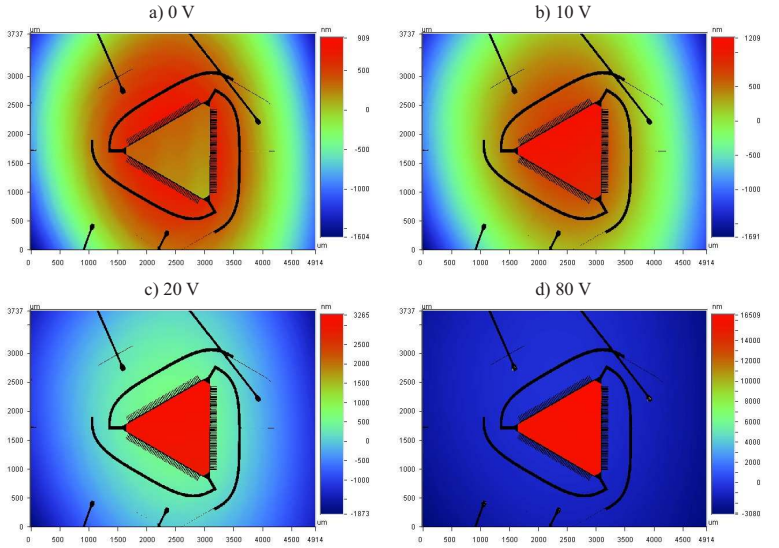

Figure 5.12: *3D topography of the vertically actuated device (piston mode) evaluated for actuation voltages of a) 0 V; b) 10 V; c) 20 V; d) 80 V. The suspension of the mirror using three curved beams results in an optically flat mirror, whereas the bow outside the mirror zone is the result of intrinsic and external stress.*

three curved suspension beams to the bulk. The indicated vertical displacements in Fig. 5.12 are in good agreement with the values measured using the optical profilometer and represented by the blue graph in Fig. 5.9. The pictures a) through d) in Fig. 5.12 show that the mirror makes a highly parallel vertical displacement without any tip-tilt. In the pictures a) through c) the bow of the die is visible due to the smaller measurement range compared to the case in picture d).

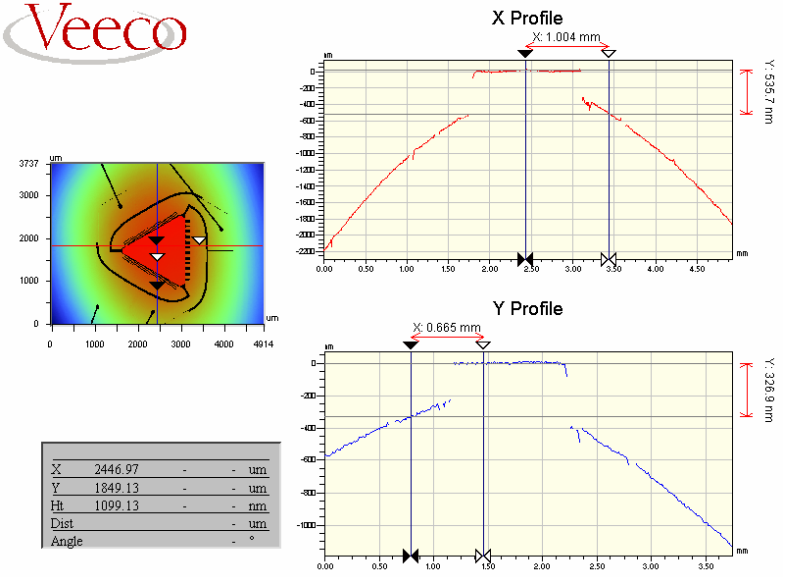

Figure 5.13: *Height profile evaluated along a line in x- and y-direction. The figure reveals the planarity of the mirror and shows that the device performs a pure piston motion in the case where an actuation voltage is applied to all three static comb electrodes.*

Piston Tip-Tilt Motion

For characterization of the piston tip-tilt motion, we applied the actuation voltage only on two static comb electrodes. The third static comb electrode and the mobile combs (i.e. the mirror) were grounded. One measurement example is shown in Fig. 5.14. In this example an actuation voltage of 50 V was applied to the two static combs that are parallel to the oblique edges of the triangular mirror.

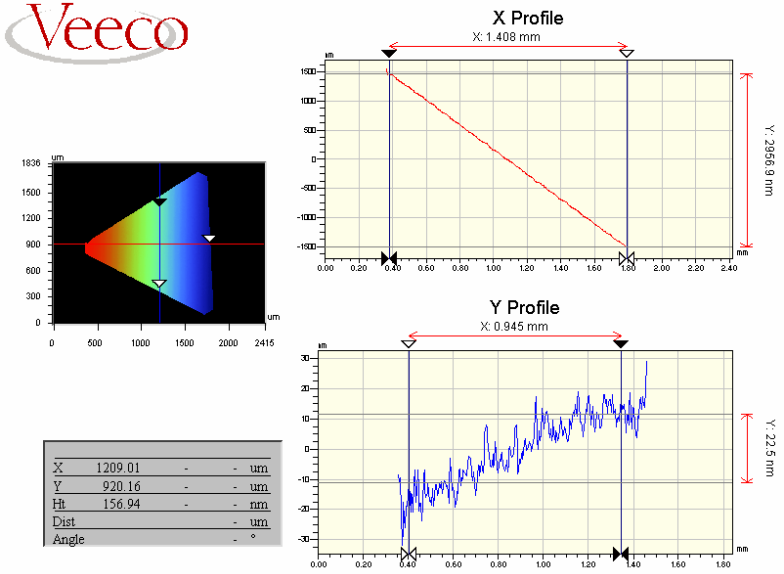

Figure 5.14: *Piston tip-tilt at 50 V actuation voltage applied on the two static combs that are parallel to the oblique edges of the mirror. Accordingly, the tilt appears only along the x-axis. The scan along the y-axis shows essentially the surface roughness. The small tilt along the y-axis is related to a bad orientation of mirror edge and scan direction.*

Voltage	Mean Δz	Tip-Tilt
0 V	0.00 µm	0.00 mrad
10 V	0.24 µm	0.12 mrad
20 V	1.73 µm	0.51 mrad
30 V	-	0.93 mrad
40 V	6.07 µm	1.64 mrad
50 V	8.22 µm	2.10 mrad

Table 5.1: *Piston tip-tilt characteristic in the case where the actuation voltage was applied on two static comb electrodes, while the third static comb electrode as well as the mobile combs were grounded.*

The x- and y-profiles were recorded along the horizontal red line and the vertical blue line, as indicated in the corresponding color map. According to the actuation scheme, the tilt appears only along the x-axis. The scan along the y-axis shows essentially the surface roughness. The small parasitic tilt along the y-axis is related to a bad orientation of mirror edge and scan direction.

In the tip-tilt mode where the actuation voltage is applied only on one or on two static comb electrodes, the mirror performs always a combined piston tip-tilt motion, i.e. a vertical displacement is superimposed on the tip-tilt. The superimposed vertical displacement gets more important for higher tip-tilt angles. The relation between tip-tilt and superimposed vertical displacement is summarized in Tab. 5.1. The tip-tilt was investigated for a maximum actuation voltage of 50 V.

Surface Flatness

In order to evaluate the impact of the stress-compensating suspension mechanism onto the bow of the mirror, we compared the curvature of the mirror with the curvature at the border of the device. The corresponding measurements are shown in Fig. 5.15 and Fig. 5.16, respectively. The curvature of the mirror was measured

to be > 30 m, with maximum values of several hundreds of meters. The curvature varied strongly in function of the measurement position on the mirror, indicating that the curvature measurement is dominated by local surface roughness. The curvature at the border of the device was measured to be 2.55 m along the indicated horizontal (red) line, and 4.86 m along the indicated vertical (blue) line. Compared to the mirror, the curvature at the edge of the device is almost one order of magnitude higher. This shows that the concept of a stress-compensating suspension mechanism works well.

In Fig. 5.16 one can notice that the curvature is more pronounced along the horizontal (red) line than along the vertical (blue) line.

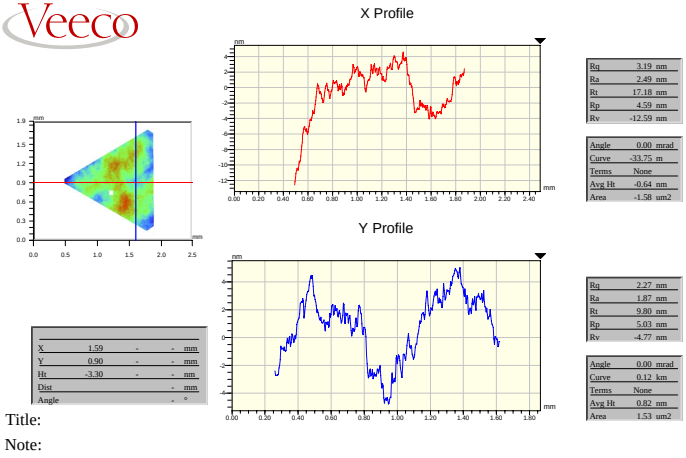

Figure 5.15: *The curvature of the mirror is roughly one order of magnitude smaller than the curvature at the border of the device (see Fig. 5.16). This demonstrates the working principle of the stress-compensating suspension mechanism.*

It has to be mentioned that the investigated die was glued onto a PCB using a two component epoxy that was applied at the four corners of the die. The epoxy was cured at 80° C for 30 min which might have caused stress due to thermal expansion of the PCB. The size of the investigated die was 12 mm in horizontal direction, and 5 mm in vertical direction. Hence, the absolute thermal expansion of the PCB is higher in the horizontal direction (12 mm edge length) which corresponds well with the measured higher curvature in this direction.

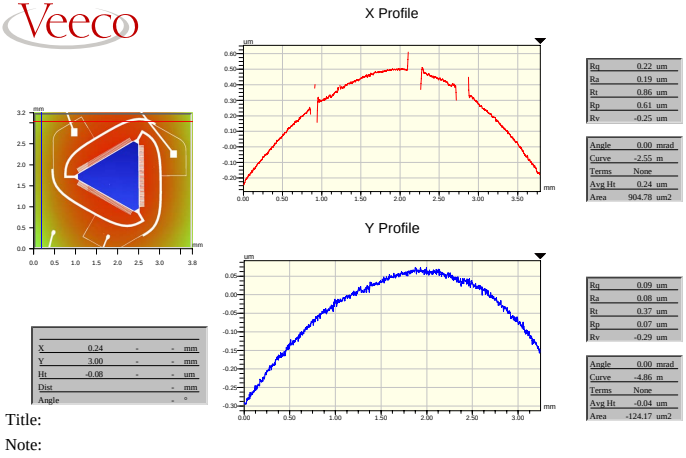

Figure 5.16: *Curvature at the border of a device which is glued onto a PCB. The different curvatures along the horizontal and the vertical axes correlate well with the ratio of chip length and width, indicating that the thermal expansion of the PCB is a potential source of stress.*

Surface Roughness

The surface roughness of the triangular mirror was measured using the phase shift interferometric (PSI) mode providing high accuracy in the subnanometer range. We evaluated an average root mean square roughness (R_{rms}) of 3.44 nm, with a maximum peak-valley elevation (R_t) of 27.52 nm.

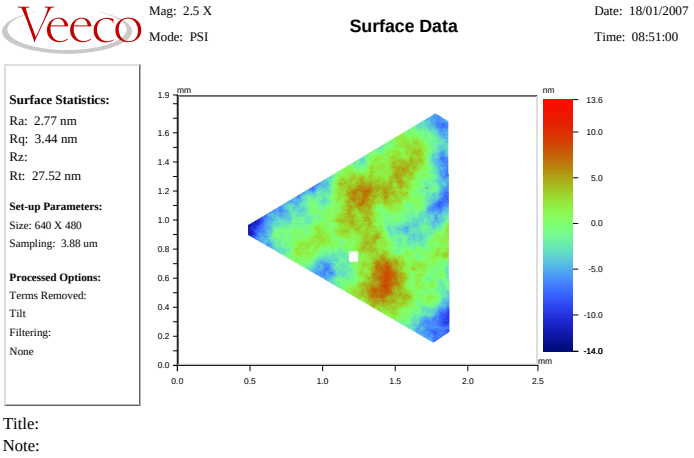

Figure 5.17: *Surface roughness of the triangular mirror. The data in the white rectangle have been removed since they were altered by a dust particle sticking to the mirror.*

Chapter 6

Conclusion

The aim of this work was the development and realization of MEMS devices providing accurate vertical displacements for tuning purpose of optical components. The actuation mechanism is based on vertical electrostatic comb drives which complement the well known electrostatic comb actuators used for in-plane actuation. In the two realized projects, the vertical electrostatic comb drives have been implemented once as vertically staggered comb actuator, and once as asymmetric vertical comb actuator. The technological realization of the two devices is based on double sided DRIE of SOI substrates.

In the first project a single axis tilting platform device was realized. The tilting platform measures $2\times2\,\mathrm{mm}^2$ and is suspended with two torsion bars. The platform can be assembled with an optical component whose angular characteristic can be changed by tilting the platform. The platform is equipped with a large hole for optical transmission. Tilting of the platform is accomplished with two sets of vertically staggered comb actuators that are arranged along two opposite edges of the platform. The vertically staggered comb actuator is built by the mobile combs located in the device layer, and the static combs located in the handle layer.

Initial problems with parasitic in-plane rotation of the platform

at elevated actuation voltages could be solved by replacing the regular straight torsion beams by novel hourglass-shaped torsion beams which were found to suppress in-plane rotation 3-5 times better than straight torsion beams. Hence, the voltage range of stable operation could be increased by several tens of volts such that we achieved finally a tilt angle of $\pm 3.5^\circ$ at 80 V. For demonstration purpose a resonant grating filter working in the telecom C-band (1530-1570 nm) was assembled on top of the platform. We successfully demonstrated tuning of the entire C-band, with a tuning accuracy better than 0.1 nm. The corresponding tilting accuracy of 0.02° outperformed the required precision imposed by the filter.

In order to avoid braking of the fragile torsion bars when dicing the wafers, we developed a new chip release process. In this process the chips are separated from each other by a combination of surrounding trenches etched by DRIE, and underetching of the buried silicon dioxide using HF vapor etching. This enabling technique substantially increased the yield and has become a standard process for many other projects inside and outside the University of Neuchâtel.

The main issue which needs to be further improved concerns the stability of the platform at high actuation voltages, although major improvements have already been achieved using hour-glass-shaped torsion beams. The reduction of notching observed in the static combs could potentially help to achieve the required tilt angle at a lower actuation voltage. Increasing the gap between the mobile and the static combs is another way to reduce in-plane rotation, at the cost of less force which would require additional combs. Nevertheless, the alignment accuracy between the mobile combs in the device layer and the static combs in the handle layer remains critical.

In the second part of this work a piston tip-tilt mirror device was realized. The original motivation for the second project was the question how the shape and the configuration of the suspension beams can contribute to more lateral stability. We also sought a design that limits stress in the suspension beams. This is important in applications requiring very flat mirrors since stress in the suspension

beams often results in small deformations of the mirror at the attachment points of the beams. Optically flat mirrors providing accurate vertical displacements have a wide application range in tunable cavity systems (e.g. interferometers, lasers, filters) and beam steering devices (e.g. scanners, deformable mirrors for adaptive optics).

In the realized device, we have achieved an optically flat mirror using a novel stress-compensating suspension mechanism. The suspension mechanism employs three C-shaped beams that are attached at the three corners of a triangular mirror. The curved shape and the arrangement of the beams allow a high vertical displacement and provide excellent lateral stability of the mirror. The actuation is performed with asymmetric vertical comb drives that are arranged along the three sides of the mirror. The mobile and the static combs are located in the device layer. The required vertical offset between the mobile and the static combs is achieved by reducing the height of the mobile combs over the height of the static combs in DRIE using a self-aligned two level mask process. The self-alignment feature avoids any misalignment between mobile and static combs, a fact that improves considerably the range of stable operation of the device.

The mirror flatness and roughness were analyzed with an optical profiler. The radius of curvature of the stress-released mirror was evaluated to be $> 30\,\mathrm{m}$, compared to 3-5 m outside the mirror zone. The average roughness (R_{rms}) of the mirror was measured to be 3.5 nm. The mirror can be lifted up individually at one, two or three sides, providing thus true 3D positioning of the mirror within the mechanical limitations. In the piston mode we achieved a highly parallel vertical displacement of up to $18\,\mu\mathrm{m}$ at 80 V. In the combined piston tip-tilt mode we measured a tip-tilt of up to 2.1 mrad at 50 V, with a superimposed mean vertical displacement of $8.2\,\mu\mathrm{m}$. The tip-tilt feature allows to correct small wedge errors related to potential dust inclusion in the packaging process.

The large vertical displacement of up to $18\,\mu\mathrm{m}$ in the piston mode has exceeded by far our expectations. To our knowledge, this is the highest reported vertical displacement realized with this type

of actuator. The achieved optical performance is excellent. The most important limitation of the device is related to the rather small tip-tilt. Future developments should address the implementation of larger tip-tilt angles in the range of several degrees in order to extend the field of potential applications. The current configuration with three comb actuators arranged along the edges of the triangular mirror do not allow higher tip-tilt angles since the mobile combs would touch the static combs.

Acknowledgements

In this section I would like to thank all the people who contributed with their advice, discussions, know-how and help to the successful realization of this work. First of all I would like to thank Prof. Nico de Rooij who gave me the opportunity to work in his enthusiastic team, for creating a research environment of highest quality, and for his support and encouragement.

I would particularly like to express my gratitude to my advisor Wilfried Noell who taught me being a scientist, and who contributed with many brilliant ideas to this work. I also like to thank the whole optical MEMS group, Michael Zickar, Yves Pétremand, Severin Waldis, and Winston Sun, for the fruitful collaboration and the many interesting discussions. I would like to particularly thank Michael Zickar for building the HF vapor phase etcher. This instrument was the basis for a non-destructive chip release process and maybe rescued the project at a very critical point.

I am very grateful to Guido Niederer who simulated and designed the resonant grating filter. The collaboration with him and with Hans Peter Herzig was always excellent.

This work has been realized in collaboration with the Swiss Center for Electronics and Microtechnology (CSEM SA). I would like to express my gratitude to Samuel Obi who built the set-up for assembly of the resonant grating filters on the MEMS titling platform, and to Hans Thiele who built the miniaturized test bench as well as the optical set-up used to analyze the MEMS tunable filter de-

vice. I also like to thank Mike Gale and Ross Stanley who guided the two projects on the CSEM side and who critically corrected my conference contributions. The financial support by CSEM is greatly acknowledged.

I would like to express my gratitude to the whole COMLAB staff, Edith Millotte, Gianni Mondin, Nicole Hegelbach, Sylvain Jeanneret, Sylviane Pochon, José Vaquera, Stéphane Ischer, and Pierre-André Clerc, for supporting my ideas, and for the great work they did on my projects. Many thanks also to Claudio Novelli for restoring several times accidentally deleted data.

I would like to thank the persons with whom I shared my office the most of my thesis time: Laure Aeschimann (remember the F1 race in Hungary!), and Giovanni Bergonzi who entertained us every day. His jokes, amazing phone calls and sense of humor made the days in the office bright. Thanks also to Winston Sun for his funny stories about loosing his bike.

Many thanks to Roman Merz who helped me a lot to get my thesis written in LaTeX.

Publications

List of Publications

[1] T. Overstolz, W. Noell, R. Stanley, and N. F. de Rooij, "Compact and Stress-Released Piston Tip-Tilt Mirror". In "Digest of the 19th IEEE Int. Conf. on Micro Electro Mechanical Systems", pp. 758–761, 2006.

[2] W. Noell, T. Overstolz, R. Stanley, and N. de Rooij, "Microactuator having beams with curved segments". European Patent Application, EP1746071A1, January 2007.

[3] T. Overstolz, G. Niederer, W. Noell, H. P. Herzig, M. T. Gale, S. Obi, H. Thiele, and N. F. de Rooij, "MEMS Tilting Platform for Filter Tuning in Optical Telecom". In "Digest of the Eurosensors XVIII Conference", pp. 327–328, 2004.

[4] T. Overstolz, G. Niederer, W. Noell, H. P. Herzig, M. T. Gale, S. Obi, H. Thiele, and N. F. de Rooij, "MEMS Tilting Platform for Filter Tuning in Optical Telecom". In "Digest of the IEEE / LEOS Int. Conf. on Optical MEMS", pp. 10–11, 2004.

[5] T. Overstolz, G. Niederer, W. Noell, M. T. Gale, H. P. Herzig, S. Obi, H. Thiele, and N. F. de Rooij, "MEMS tunable filter for telecom applications". In "MEMS, MOEMS, and Micromachin-

ing", volume 5455, pp. 240–251, SPIE, 2004.
URL http://link.aip.org/link/?PSI/5455/240/1

[6] T. Overstolz, P. A. Clerc, W. Noell, M. Zickar, and N. F. de Rooij, "A Clean Wafer-Scale Chip-Release Process without Dicing Based on Vapor Phase Etching". In "Digest of the 17th IEEE Int. Conf. on Micro Electro Mechanical Systems", pp. 717–720, 2004.

[7] O. Manzardo, R. Michaely, F. Schädelin, W. Noell, T. Overstolz, N. F. de Rooij, and H. P. Herzig, "Miniature lamellar grating interferometer based on silicon technology". *Opt. Lett.*, **29**:1437–1439, 2004.

[8] M. T. Gale, W. Noell, T. Overstolz, and H. Thiele, "Linear response MEMS device". UK Patent Application, GB2389707A, December 2003.

[9] O. Manzardo, R. Michaely, F. Schädelin, H. P. Herzig, W. Noell, T. Overstolz, and N. F. de Rooij, "Micro-sized Spectrometer Based on a Lamellar Grating Interferometer". In "Digest of the IEEE / LEOS Int. Conf. on Optical MEMS", pp. 175–176, 2003.

[10] L. Berdondini, T. Overstolz, M. Koudelka-Hep, and P. Seitz, "High density microelectrode arrangement". European Patent Application, EP1278064A1, January 2003.

[11] T. Overstolz, P.-A. Clerc, M. T. Gale, H. P. Herzig, G. Niederer, W. Noell, H. Thiele, and N. F. de Rooij, "Tilting Out-Of-Plane Platform for Optical Applications". In "Digest of the IEEE / LEOS Int. Conf. on Optical MEMS", pp. 81–82, 2002.

[12] L. Berdondini, T. Overstolz, N. F. de Rooij, M. Koudelka-Hep, S. Martinoia, P. Seitz, M. Wäny, and N. Blanc, "High resolution electrophysiological activity imaging of in-vitro neuronal networks". In "Proc. IEEE-EMB Int. Conf. on Microtechnologies in Medicine and Biology", pp. 241–244, 2002.

[13] L. Berdondini, T. Overstolz, N. de Rooij, M. Koudelka-Hep, M. Wäny, and P. Seitz, "High-density microelectrode arrays for electrophysiological activity imaging of neuronal networks". In "Proc. 8th IEEE Int. Conf. on Electronics, Circuits and Systems", volume 3, pp. 1239–1242, 2001.